



Contents lists available at ScienceDirect

## Arabian Journal of Chemistry

journal homepage: [www.ksu.edu.sa](http://www.ksu.edu.sa)

Original article



# Magnetoplasmonic core-shell structured Ag@Fe<sub>3</sub>O<sub>4</sub> particles synthesized via polyol reduction process rendering dual-functionality for bacteria ablation and dyes degradation

Qing Shen<sup>a</sup>, Luping Zhang<sup>c</sup>, Yuan Zhao<sup>b</sup>, Xiaobing Han<sup>b</sup>, Jie Gao<sup>b</sup>, Yuesheng Li<sup>b</sup>, Xiaoming Zhu<sup>b</sup>, Tian Liang<sup>b,\*</sup>, Tao Chen<sup>b,\*</sup>

<sup>a</sup> School of Pharmacy, Hubei University of Science and Technology, Xianning 437100, China

<sup>b</sup> Hubei Key Laboratory of Radiation Chemistry and Functional Materials, School of Nuclear Technology and Chemistry & Biology, Hubei University of Science and Technology, Xianning 437100, China

<sup>c</sup> School of Education, Hubei University of Science and Technology, Xianning 437100, China

## ARTICLE INFO

## Keywords:

Magnetoplasmonic  
Core shell structure  
Ag  
Fe<sub>3</sub>O<sub>4</sub>  
Antibacterial  
Catalytic degradation  
Organic dyes

## ABSTRACT

The Ag nanoparticles demonstrate potent bacteria eradication capabilities; however, their tendency to aggregate in aqueous solutions compromises the antibacterial efficacy. Furthermore, the Ag nanoparticles employed in sewage treatment are challenging to recycle, resulting in environmental pollution and resource wastage. Herein, the Ag-core Fe<sub>3</sub>O<sub>4</sub>-shell structured particles (Ag@Fe<sub>3</sub>O<sub>4</sub>) are synthesized by leveraging the reduction potential difference between Ag<sup>+</sup>/Ag<sup>0</sup> and Fe<sup>3+</sup>/Fe<sup>2+</sup> through a one-step polyol reduction process. The Fe<sub>3</sub>O<sub>4</sub> shell in the Ag@Fe<sub>3</sub>O<sub>4</sub> composite not only effectively inhibits the agglomeration of Ag, but also enhances the penetration capability of the composite into biofilms, thereby enabling Ag@Fe<sub>3</sub>O<sub>4</sub> to possess remarkable antibacterial efficacy against *Escherichia coli* (*E. coli*). The Ag@Fe<sub>3</sub>O<sub>4</sub> demonstrates nearly 100 % inhibition of *E. coli* at a concentration of 0.24 mg mL<sup>-1</sup> (with an Ag content of 0.042 mg mL<sup>-1</sup>) while still maintaining antibacterial effectiveness of 74.6 % even after undergoing reutilization for 10 cycles. Meanwhile, due to the excellent electron conductivity of Ag and the effective adsorption capability of Fe<sub>3</sub>O<sub>4</sub> shell towards organic dyes, Ag@Fe<sub>3</sub>O<sub>4</sub> facilitates rapid electron transfer to organic dyes and further lead to their reduction and degradation in the presence of NaBH<sub>4</sub>. The Ag@Fe<sub>3</sub>O<sub>4</sub> can catalytically degrade various organic dyes (including Rhodamine B, Rhodamine 6G, and Methylene blue) within only 15 min, while achieving an impressive degradation efficiency exceeding 90.9 % after 6 cycles of reutilization. The cost-effectiveness (approximately \$0.17 per gram), facile magnetic recovery, along with the superior antibacterial and dye-degradation performance showcase the significant potential of Ag@Fe<sub>3</sub>O<sub>4</sub> for medical applications and sewage treatment.

## 1. Introduction

The overuse of antibiotics in recent years has accelerated the evolution of bacteria, resulting in the emergence of antibiotic-resistant “superbugs” that pose a significant threat to human health (Jia et al., 2017; Salam et al., 2023). The development of highly efficient and environmentally friendly new antibacterial materials is therefore urgently needed. The remarkable antibacterial properties of metal ions have attracted significant attention, with silver (Ag) standing out for its exceptional antibacterial activity compared to other metals (Ag > Hg > Cu > Cd > Cr > Ni > Pb > Co > Zn > Fe > Ca) (Berger et al., 1976;

Fouladi-Fard et al., 2022; Razavi et al., 2021). However, conventional methods of synthesizing silver nanoparticles often result in agglomeration, leading to a significant decrease in their antibacterial efficacy (Ye et al., 2019; Zeng et al., 2018; Zhao et al., 2017).

To address the issue of agglomeration of silver nanoparticles, numerous investigations have been undertaken. Gankhuyag et al. synthesized silica-supported silver nanoparticles (SiO<sub>2</sub>@Ag) by impregnating silica particles (100–130 nm) in an AgNO<sub>3</sub> solution using trisodium citrate as a reducing agent, which exhibited remarkable antibacterial activity against *E. coli* (Gankhuyag et al., 2021). Ghosh et al. developed the TiO<sub>2</sub>-Ag nanocomposite through mechanical

\* Corresponding authors.

E-mail addresses: [liangtian@hbust.edu.cn](mailto:liangtian@hbust.edu.cn) (T. Liang), [taochen518@163.com](mailto:taochen518@163.com) (T. Chen).

<https://doi.org/10.1016/j.arabjc.2024.106058>

Received 1 July 2024; Accepted 8 November 2024

Available online 9 November 2024

1878-5352/© 2024 Published by Elsevier B.V. on behalf of King Saud University. This is an open access article under the CC BY-NC-ND license (<http://creativecommons.org/licenses/by-nc-nd/4.0/>).

alloying of TiO<sub>2</sub> and Ag powder under an Ar atmosphere, resulting in significantly enhanced photocatalytic and antibacterial activities (Ghosh et al., 2020). Cinteza et al. employed an electrochemical method with a sacrificial anode to synthesize the Ag nanoparticles, further utilizing chitosan as a capping agent to enhance stabilization and biocompatibility while preserving antibacterial activity (Cinteza et al., 2018). Yang et al. fabricated the C-Zn/Ag nanocomposite by introducing Ag nanoparticles into a MOF-derived carbonized framework containing metallic Zn, which can rapidly release Ag<sup>+</sup> ions to inactivate bacterial intracellular proteins (Yang et al., 2020).

Although much progress has been made, one challenge lies in the difficulty of recycling the nanoparticles during utilization, which could potentially result in environmental pollution and resource wastage (Mohajerani et al., 2019; Chaukura et al., 2016; Islam et al., 2021). To achieve the objectives of environmental conservation and sustainable development, we synthesized the Ag-core Fe<sub>3</sub>O<sub>4</sub>-shell structured particles (Ag@Fe<sub>3</sub>O<sub>4</sub>) by leveraging the reduction potential difference between Ag<sup>+</sup>/Ag<sup>0</sup> and Fe<sup>3+</sup>/Fe<sup>2+</sup> through a one-step polyol reduction process. The magnetoplasmonic core-shell Ag@Fe<sub>3</sub>O<sub>4</sub> nanoparticles, which can be easily synthesized, not only prevent the agglomeration of Ag but also facilitate their effortless recovery. The Ag@Fe<sub>3</sub>O<sub>4</sub> nanoparticles demonstrate exceptional antibacterial performance due to the well-dispersed Ag and sustained release of Ag<sup>+</sup> through the porous Fe<sub>3</sub>O<sub>4</sub> shell. At a concentration of 0.24 mg mL<sup>-1</sup> (with an Ag content of 0.042 mg mL<sup>-1</sup>), the Ag@Fe<sub>3</sub>O<sub>4</sub> exhibit nearly 100 % inhibition against *E. coli*, while maintaining a significant antibacterial efficacy of 74.6 % even after undergoing reutilization for 10 cycles. In addition to the antibacterial properties, the Ag@Fe<sub>3</sub>O<sub>4</sub> nanoparticles also demonstrate exceptional catalytic degradation capabilities in the presence of NaBH<sub>4</sub> towards organic dyes owing to their intricate characteristics and delicate nanostructure. The organic dye molecules are adsorbed onto the active sites on the Fe<sub>3</sub>O<sub>4</sub> shell (possibly through electrostatic attraction and van der Waals force) while the electron transfer mediator of Ag facilitates efficient electron transfer from the nucleophilic NaBH<sub>4</sub> to the electrophilic dye molecules, ultimately inducing reduction and degradation of the dye molecules (Amir et al., 2015; Zhang et al., 2017; Shi et al., 2021). The Ag@Fe<sub>3</sub>O<sub>4</sub> can catalytically degrade various organic dyes (including Rhodamine B, Rhodamine 6G, and Methylene blue) within just 15 min, and also achieve a degradation efficiency of over 90.9 % after undergoing 6 cycles of reutilization.

Overall, the cost-effectiveness (approximately \$0.17 per gram), facile magnetic recovery, antibacterial property, and catalytic degradation towards organic dyes render Ag@Fe<sub>3</sub>O<sub>4</sub> particles a promising candidate for large-scale applications in antibacterial treatments and waste water treatment.

## 2. Materials and methods

### 2.1. Chemical reagents

Fe(NO<sub>3</sub>)<sub>3</sub>·9H<sub>2</sub>O was purchased from Shanghai Yien Chemical Technology Co. Ltd. AgNO<sub>3</sub>, ethylene glycol, sodium acetate (NaAc), oxalic acid, NaBH<sub>4</sub>, and Methylene blue (MB) were obtained from Sinopharm Chemical Reagent Co. Ltd., China. Rhodamine B (RB) and Rhodamine 6G (R6G) were purchased from Shanghai McLin Biochemical Technology Co., Ltd. Beef infusion powder, tryptone, yeast powder, and AGAR powder were sourced from Beijing Lan Ji Ke Technology Co., LTD. *Escherichia coli* (*E. coli*) strain was acquired from Hai Bo Biotechnology Limited.

### 2.2. Synthesis of materials

#### 2.2.1. Synthesis of Ag@Fe<sub>3</sub>O<sub>4</sub>

The core-shell structured Ag@Fe<sub>3</sub>O<sub>4</sub> particles were synthesized via a one-step polyol reduction process (Dong et al., 2019; X.h. Meng, X. Shao, H.y. Li, F.z. Liu, X.p. Pu, W.z. Li, C.h. Su, One-step hydrothermal

synthesis, characterization and visible-light catalytic property of Ag-reduced graphene oxide composite, *Materials Research Bulletin* 48(4), 2013; Hou et al., 2017; Jiao et al., 2018; Liang et al., 2023). Specifically, Fe(NO<sub>3</sub>)<sub>3</sub>·9H<sub>2</sub>O (1.212 g), sodium acetate (2.153 g), and AgNO<sub>3</sub> (0.076 g) were sequentially added to ethylene glycol (30 ml) and stirred for 30 min. The resulting mixture was then transferred into a Teflon-lined stainless-steel autoclave and heated at 200 °C for 4 h. Finally, the product was washed three times with deionized water, subjected to centrifugation, and dried at 60 °C overnight to obtain the Ag@Fe<sub>3</sub>O<sub>4</sub> particles.

#### 2.2.2. Synthesis of solid Ag cores (c-Ag)

The Ag@Fe<sub>3</sub>O<sub>4</sub> was immersed in a 1 mol L<sup>-1</sup> oxalic acid solution overnight, resulting in the formation of ferric oxalate and a yellow-green solution due to the reaction between Fe<sub>3</sub>O<sub>4</sub> and oxalic acid, thus obtaining the c-Ag (Shrivastava et al., 2022; Yu et al., 2018; Zhang et al., 2014).

#### 2.2.3. Synthesis of hollow Fe<sub>3</sub>O<sub>4</sub> shells (s-Fe<sub>3</sub>O<sub>4</sub>)

The Ag@Fe<sub>3</sub>O<sub>4</sub> was immersed in a 0.1 mol L<sup>-1</sup> Fe(NO<sub>3</sub>)<sub>3</sub> solution and subjected to ultrasonication for 30 min. Afterwards, it was rinsed with deionized water three times and finally dried, resulting in the formation of s-Fe<sub>3</sub>O<sub>4</sub> (Chen et al., 2014; Lu et al., 2007; Zhang et al., 2018).

### 2.3. Materials characterization

The morphology and microstructure of the samples were observed using a Field Emission Scanning Electron Microscope (FE-SEM, SU8010, Hitachi, Japan) and a Transmission Electron Microscope (TEM, FEI Tecnai G2 F20 S-TWIN, FEI, USA). The Atomic Absorption Spectrometer (AAS, PinAAcle 900F, Perkin Elmer, USA) is utilized for the determination of the elemental composition of materials. The Dynamic Light Scattering (DLS, Zetasizer Nano ZS90, Malvern, UK) is employed for the analysis of particle size distribution and polydispersity index (PDI) of the Ag@Fe<sub>3</sub>O<sub>4</sub> particles. The crystal structure of the samples was analyzed using D8-FOCUS powder X-ray diffraction (XRD, D8-FOCUS, Bruker, Germany) with Cu Kα target (λ = 0.154 nm) at a voltage of 40 KV, a current of 35 mA, and a scanning speed of 10° min<sup>-1</sup>. The absorption peaks of the samples were determined using an Ultraviolet-Visible Spectrophotometer (UV, 1901 PC, Shanghai AUCY, China) with a scanning range from 200 to 800 nm. The Brunauer-Emmett-Teller (BET, ASAP 2460, Micromeritics, USA) measurements were utilized to measure the specific surface area of materials, while the pore size distribution of the materials was determined utilizing the Barrett-Joyner-Halenda (BJH) model. The magnetization curves of the samples were measured using a Vibrating Sample Magnetometer (VSM, 7404, Lake Shore, USA). Fourier Transform Infrared Spectroscopy (FT-IR, Spectrum two, Perkin Elmer, USA) was employed to analyze the composition and structural information of the materials. The X-ray Photoelectron Spectrometer (XPS, K-Alpha, thermo scientific, USA) is utilized for the validation of the electronic state and chemical composition of the materials. The Electron Spin Resonance (ESR, EMXplus-6/1, Bruker, Germany) is used to qualitatively and quantitatively detect the unpaired electrons present in atoms or molecules of materials.

### 2.4. Antibacterial experiments

This study assesses the antibacterial efficacy of the samples using *E. coli* as the test bacteria. Liquid medium preparation: a solution containing peptone (2 g), beef extract (0.6 g), and NaCl (1 g) dissolved in distilled water (200 ml) was sterilized at 121 °C for 30 min. Solid medium preparation: a mixture containing peptone (2 g), yeast extract (1 g), NaCl (2 g), and agar (3 g) dissolved in distilled water (200 ml) was sterilized at 121 °C for 30 min. *E. coli* activation: *E. coli* liquid (1 mL) was inoculated into liquid medium (200 mL) and incubated overnight at 37 °C in a constant temperature oscillator (Shakoori and Muneer, 2002).

#### 2.4.1. Measurement for the diameter of inhibition zone (DIZ)

The activated *E. coli* was first diluted to a concentration of  $5 \times 10^6$  Colony-Forming Units (CFU) per milliliter using physiological saline. Subsequently, 100  $\mu\text{L}$  of the diluted *E. coli* suspension was evenly spread onto the solid culture medium and placed within an Oxford cup. The c-Ag, s- $\text{Fe}_3\text{O}_4$ , and Ag@ $\text{Fe}_3\text{O}_4$  suspensions at various concentrations were placed in separate Oxford cups and incubated at 37 °C for 12 h prior to measuring the diameter of the inhibition zone (Aldosari et al., 2023; Xiong et al., 2013).

#### 2.4.2. Measurement of the minimum inhibitory concentration (MIC)

The MIC refers to the minimum antibacterial concentration that can inhibit bacterial growth (Tang and Zheng, 2018; Mei et al., 2014). A negative control group (only broth) and a positive control group (mixture of bacteria and broth) were set up for comparison. The synthesized particles of various weight (1–10 mg), bacterial solution (100  $\mu\text{L}$  with a concentration of  $10^6$  colony forming units (CFU) per mL), and liquid broth (25 mL) were mixed thoroughly and cultured in a constant temperature incubator at 37 °C for 10 h. When the concentration of the composite material in the test tube surpasses the MIC, it effectively impedes bacterial growth and reproduction, resulting in a visibly clear solution within the test tube. Conversely, if the concentration of the composite material is below the MIC, it fails to hinder bacterial reproduction and growth, leading to a persistently turbid solution. Therefore, the MIC value of the composite material can be determined by visually observing the turbidity change in the test tube solution before and after incubation (Parvekar et al., 2020).

#### 2.4.3. Cyclic antibacterial ability

The synthesized particles (10 mg) and a fresh bacterial solution (5 mL at a concentration of  $10^6$  CFU per mL) were introduced into a sterile reagent bottle and thoroughly mixed, followed by incubation at room temperature for 150 min. The above suspension was subjected to magnetic separation, and the supernatant containing bacteria (100  $\mu\text{L}$ ) was extracted. Subsequently, it was diluted 1000-fold with normal saline before being spread onto solid medium and incubated at 37 °C for 24 h. The colony count was subsequently conducted, followed by the calculation of the bacterial inhibition rate. This was denoted as the first cycle of the antibacterial experiment. After the aforementioned magnetic separation process, the residual bacterial solution was discarded, and the unwashed separated particles were mixed with another fresh bacterial solution (5 mL at a concentration of  $10^6$  CFU per mL) (Yong et al., 2018). The subsequent steps were then repeated for the next cycle.

The bacterial inhibition rate is calculated as follows (Wang et al., 2020; Shuai et al., 2020):

$$R = (B - C)/B$$

where R (%) is the bacterial inhibition rate, B denotes the colony count in the control experiment without any treatment, and C represents the colony count after adding the Ag@ $\text{Fe}_3\text{O}_4$ .

### 2.5. Catalytic degradation experiments

The organic dyes of Rhodamine B (RB), Rhodamine 6G (R6G), and Methylene blue (MB) exhibit responsiveness to UV–visible (UV–vis) light, and the intensity of their absorption peaks demonstrates a positive correlation with concentration according to the Beer-Lambert Law. Therefore, the concentration of the organic dyes can be effectively monitored by employing UV–vis spectrophotometry. The synthesized particles (20 mg) were dispersed in an aqueous solution of organic dyes (RB, R6G, MB; 20 mL, 5 mg  $\text{L}^{-1}$ ) under continuous agitation, followed by the addition of sodium borohydride (1.5 mg). The catalytic degradation activity of the particles was assessed by monitoring changes in dye concentration through measuring variations in the main absorbance peak within the UV–vis spectrum.

The degradation rate (R) is calculated as follows (Sakir and Onses, 2019; Hao et al., 2013):

$$R = (C_0 - C_t)/C_0$$

where  $C_0$  (mg  $\text{L}^{-1}$ ) and  $C_t$  (mg  $\text{L}^{-1}$ ) represent the initial and residual concentration of the dyes, respectively. The recyclability of the samples was evaluated by conducting repeated experiments as described above. After each cycle, the samples were separated using a magnet and then subjected to another round of testing. The recyclable catalytic efficiency corresponds to the degradation rate calculated in each cycle.

## 3. Results and discussion

The synthesis procedure of Ag@ $\text{Fe}_3\text{O}_4$  core-shell nanoparticle involves a polyol reduction process by a solvothermal approach (Fig. 1). Specifically,  $\text{AgNO}_3$  and  $\text{Fe}(\text{NO}_3)_3 \cdot 9\text{H}_2\text{O}$  are dissolved in ethylene glycol along with sodium acetate, forming a clear solution. The mixture is then transferred to an autoclave and heated at 200 °C for 4 h to obtain the Ag@ $\text{Fe}_3\text{O}_4$  composite. Due to the higher standard hydrogen electrode (SHE) potential of  $\text{Ag}^+/\text{Ag}^0$  ( $E_{\text{Ag}^+/\text{Ag}^0} = +0.799\text{V vs. SHE}$ ) compared to that of  $\text{Fe}^{3+}/\text{Fe}^{2+}$  ( $E_{\text{Fe}^{3+}/\text{Fe}^{2+}} = +0.77\text{V vs. SHE}$ ), the reduction rate of  $\text{Ag}^+$  to  $\text{Ag}^0$  surpasses that of  $\text{Fe}^{3+}$  to  $\text{Fe}^{2+}$ , leading to the initial formation of Ag cores which serve as seeds for the subsequent deposition of  $\text{Fe}_3\text{O}_4$  shells (Zhang et al., 2012). The formation of  $\text{Fe}_3\text{O}_4$  (magnetite) shells involves a specific redox process where  $\text{Fe}^{3+}$  is partially reduced to  $\text{Fe}^{2+}$  in the presence of polyol. After the partial reduction of  $\text{Fe}^{3+}$  to  $\text{Fe}^{2+}$ , the  $\text{Fe}^{2+}$  and the remaining  $\text{Fe}^{3+}$  ions in the solution combine together and result in the precipitation of  $\text{Fe}_3\text{O}_4$  as a solid under alkaline conditions. During the reaction process,  $\text{AgNO}_3$  and  $\text{Fe}(\text{NO}_3)_3 \cdot 9\text{H}_2\text{O}$  provide the necessary metal ions for the formation of Ag cores and  $\text{Fe}_3\text{O}_4$  shells, respectively. Ethylene glycol plays a pivotal role as a reducing agent, facilitating the reduction of metal ions. Sodium acetate may function as a stabilizing agent that regulates the reaction kinetics. The combination of the aforementioned chemical reagents in the solvothermal reaction ultimately results in the formation of magnetoplasmonic core-shell structured Ag@ $\text{Fe}_3\text{O}_4$  particles. Due to their intricate characteristics and delicate nanostructure, the Ag@ $\text{Fe}_3\text{O}_4$  nanoparticles possess dual functionality for bacteria ablation and dye degradation.

### 3.1. Materials characterization

#### 3.1.1. SEM and TEM analysis

The scanning electron microscope (SEM) images reveal that the Ag@ $\text{Fe}_3\text{O}_4$  particles exhibit a high degree of monodispersity, showcasing nearly spherical morphology with an average diameter of approximately 220 nm (Fig. 2a). Upon closer examination of the magnified SEM image, it becomes evident that these spheres possess a non-smooth surface with the presence of numerous small nanoparticles (Fig. 2b). The observed disparity between the inner core and outer shell in the transmission electron microscope (TEM) images of Ag@ $\text{Fe}_3\text{O}_4$  implies the presence of core/shell structures (Fig. 2c, d). In these images, the Ag cores exhibit a dark appearance while the  $\text{Fe}_3\text{O}_4$  shells appear lighter due to Ag's higher electron density, resulting in reduced electron transmission (M.E.n.F. Brollo, RománLópez-Ruiz, D. Muraca, S. J.A. Figueroa, K.R. Pirota, M. Knobel, , 2014). The silver cores demonstrate a nearly uniform size of approximately 70 nm, with multiple tiny  $\text{Fe}_3\text{O}_4$  NPs comprising the shells that possess an average thickness of around 75 nm. The high-angle annular dark-field (HAADF) image (Fig. 2e) and energy dispersive X-ray spectrometer (EDX) mapping images (Fig. 2f) of Ag@ $\text{Fe}_3\text{O}_4$  clearly demonstrate the distribution of Fe, O, and Ag within the Ag@ $\text{Fe}_3\text{O}_4$  composite, confirming the successful integration of these elements in the Ag@ $\text{Fe}_3\text{O}_4$  as well as the Ag-core  $\text{Fe}_3\text{O}_4$ -shell structure.

The morphology and microstructure of the control samples, including  $\text{Fe}_3\text{O}_4$  shells (s- $\text{Fe}_3\text{O}_4$ ) and Ag cores (c-Ag), are also examined.

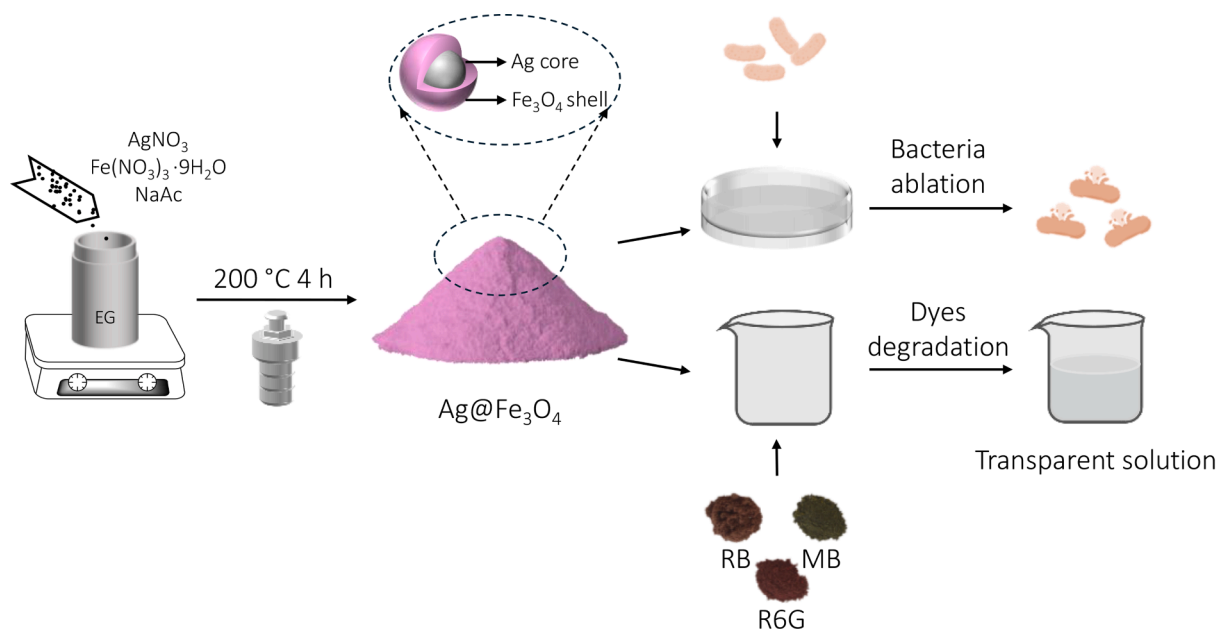


Fig. 1. The scheme of synthesizing magnetoplasmonic core-shell structured Ag@Fe<sub>3</sub>O<sub>4</sub> particles and their dual-functionality.

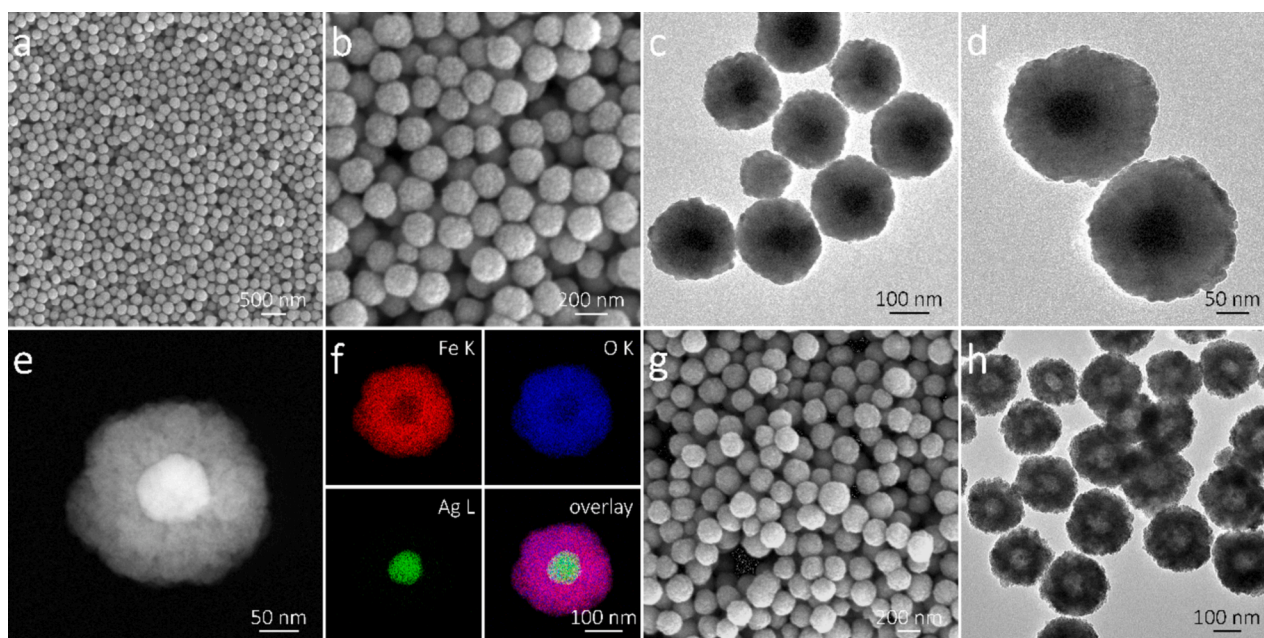


Fig. 2. (a, b) SEM, (c, d) TEM, (e) HAADF image, and (f) EDX mapping images of the core-shell structured Ag@Fe<sub>3</sub>O<sub>4</sub> nanoparticles; (g) SEM and (h) TEM images of the hollow s-Fe<sub>3</sub>O<sub>4</sub> particles.

Results indicate that s-Fe<sub>3</sub>O<sub>4</sub> exhibit a rough texture and discernible pores with a hollow structure (Fig. 2g, h), while c-Ag possess a spherical morphology (Fig. S1, Supporting Information), and their dimensions are consistent with the shell and core of Ag@Fe<sub>3</sub>O<sub>4</sub>, respectively. The weight percentages of Fe<sub>3</sub>O<sub>4</sub> and Ag in the Ag@Fe<sub>3</sub>O<sub>4</sub> are determined through the Atomic Absorption Spectroscopy analysis (Table S1, Supporting Information), which are 79.2 wt% and 20.8 wt%, respectively.

### 3.1.2. DLS analysis

The DLS technique is employed for the analysis of particle size distribution and polydispersity index (PDI) of the Ag@Fe<sub>3</sub>O<sub>4</sub> particles. The DLS pattern (Fig. 3a) reveals that the average hydrodynamic diameter of Ag@Fe<sub>3</sub>O<sub>4</sub> is 211.3 nm, which aligns with the TEM results. The detected

polydispersity index is 0.213, confirming a relatively narrow size distribution of the Ag@Fe<sub>3</sub>O<sub>4</sub> nanoparticles (Gong et al., 2007; Tayyaba et al., 2020).

### 3.1.3. XRD analysis

X-ray Diffraction (XRD) patterns provide valuable information on the crystalline structure and composition of materials. The prepared samples all exhibit distinct diffraction peaks, indicating their excellent crystallinity (Fig. 3b). The peaks of c-Ag at  $2\theta = 38^\circ, 44.2^\circ, 64.3^\circ,$  and  $77.4^\circ$  correspond to the (111), (200), (220), and (311) crystal planes of Ag, respectively, as identified by the Joint Committee of Powder Diffraction Society PDF card No. 87-0717 (Akhavan, 2009; Jeon et al., 2003; Rajesh, 2012). The peaks of s-Fe<sub>3</sub>O<sub>4</sub> at  $2\theta = 30.2^\circ, 35.5^\circ, 43.1^\circ,$

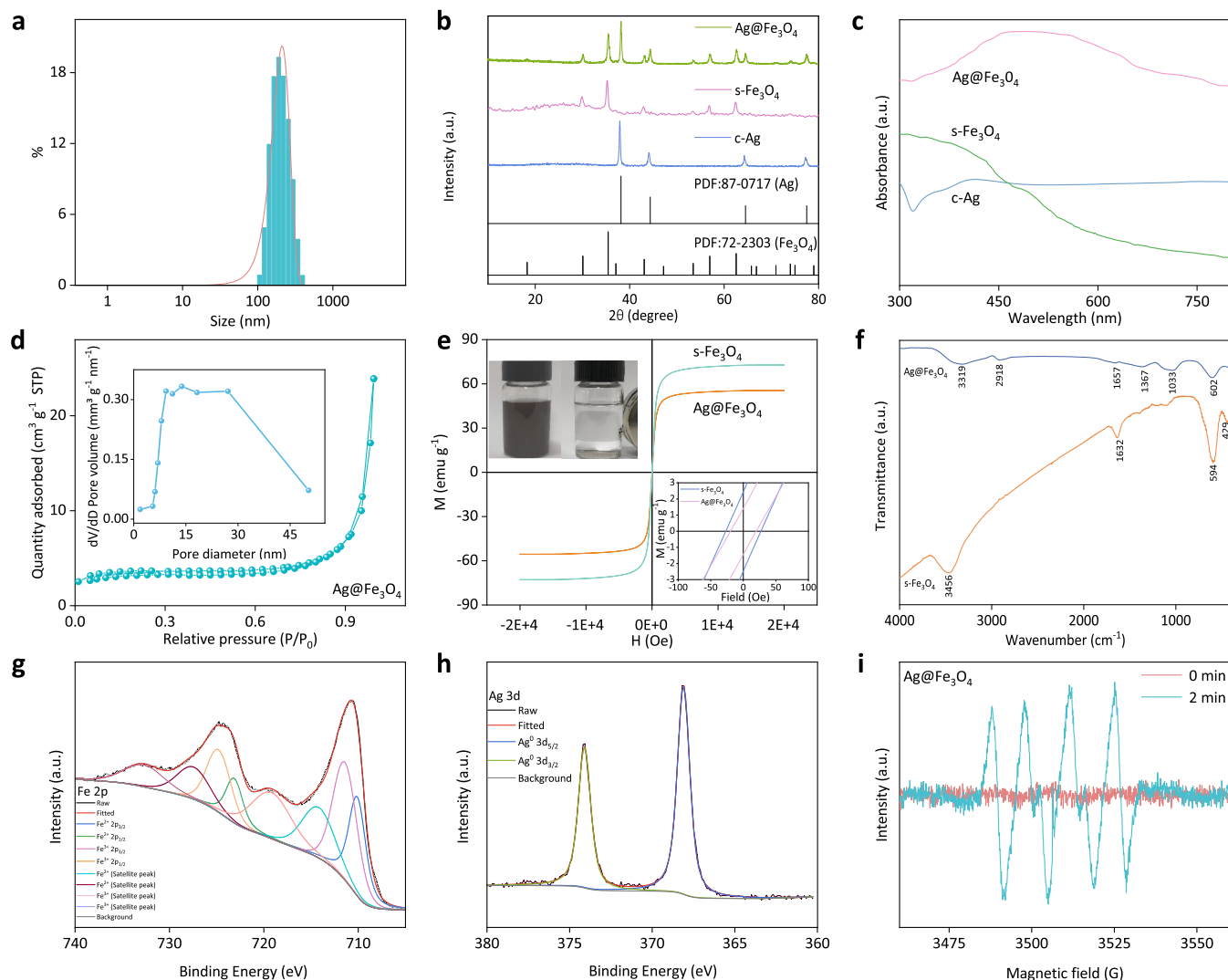


**Fig. 3.** (a) The size distribution of the Ag@Fe<sub>3</sub>O<sub>4</sub> nanoparticles; (b) XRD patterns and (c) UV–vis spectra of the c-Ag, s-Fe<sub>3</sub>O<sub>4</sub>, and Ag@Fe<sub>3</sub>O<sub>4</sub>; (d) N<sub>2</sub> adsorption/desorption isotherm and pore size distribution of the Ag@Fe<sub>3</sub>O<sub>4</sub>; (e) magnetic hysteresis loops of s-Fe<sub>3</sub>O<sub>4</sub> and Ag@Fe<sub>3</sub>O<sub>4</sub>, the insets are magnetic recovery images of Ag@Fe<sub>3</sub>O<sub>4</sub> and magnified magnetic hysteresis loops of s-Fe<sub>3</sub>O<sub>4</sub> and Ag@Fe<sub>3</sub>O<sub>4</sub>; (f) FTIR spectra of the s-Fe<sub>3</sub>O<sub>4</sub> and Ag@Fe<sub>3</sub>O<sub>4</sub>; high-resolution XPS spectra of (g) Fe 2p and (h) Ag 3d in Ag@Fe<sub>3</sub>O<sub>4</sub>; (i) ESR spectra of Ag@Fe<sub>3</sub>O<sub>4</sub> in aqueous solution at the time of 0 min and 2 min.

53.4°, 56.9°, 62.6° and 74.1° can be assigned to the (220), (311), (400), (422), (511), (440) and (533) crystal planes of Fe<sub>3</sub>O<sub>4</sub>, respectively, according to the PDF card No. 72–2303 (Wei et al., 2012; Vijayakumar et al., n.d.). The successful synthesis of Ag@Fe<sub>3</sub>O<sub>4</sub> is confirmed by the presence of both Ag and Fe<sub>3</sub>O<sub>4</sub> diffraction peaks in its pattern.

### 3.1.4. UV–vis analysis

The UV–vis spectroscopy offers valuable insights into the electronic structure of diverse materials, as the absorption of light at distinct wavelengths by different materials is attributed to their specific electronic transitions. Fe<sub>3</sub>O<sub>4</sub> primarily absorbs light in the ultraviolet (UV) region due to electronic transitions involving its d orbitals. In the visible region, Fe<sub>3</sub>O<sub>4</sub> does not have electronic transitions that coincide with the energy levels of visible light, resulting in no significant absorption peaks in this region, which is consistent with the spectrum of s-Fe<sub>3</sub>O<sub>4</sub> (Fig. 3c) (Joshi et al., 2014; Sheng and Xue, 2012). The absorption peak of c-Ag is observed at 417 nm (Chen et al., 2010; Height et al., 2006), which is attributed to the phenomenon of surface plasmon resonance (SPR), where light energy is absorbed and leads to the collective oscillation of free electrons on the surface of silver nanoparticles. The peak for Ag@Fe<sub>3</sub>O<sub>4</sub> is located at 486 nm, demonstrating a red shift in comparison to Ag. The observed outcome can be attributed to the fact that the

refractive index of Fe<sub>3</sub>O<sub>4</sub> (2.420) is higher than that of silver (0.399), resulting in a red shift of the SPR peak when silver core is coated with Fe<sub>3</sub>O<sub>4</sub> shell (Anandan et al., 2008).

### 3.1.5. BET analysis

The specific surface area and pore characteristic (Fig. 3d) of Ag@Fe<sub>3</sub>O<sub>4</sub> are determined by the BET analysis. According to the classification by the International Union of Pure and Applied Chemistry (IUPAC), the N<sub>2</sub> adsorption/desorption isotherm of Ag@Fe<sub>3</sub>O<sub>4</sub> exhibits a Type IV curve with a hysteresis loop, indicating its mesoporous structure (Zhao et al., 2011). The data analysis confirms that the Ag@Fe<sub>3</sub>O<sub>4</sub> nanoparticles exhibit a relatively high specific surface area of 13.8 m<sup>2</sup> g<sup>-1</sup> and possess abundant mesopores with an average size of 29.9 nm. The high specific surface area ensures thorough contact between the active sites on Ag@Fe<sub>3</sub>O<sub>4</sub> and the target (bacteria or organic dyes), while the abundant mesopores facilitate efficient mass transfer of Ag<sup>+</sup> or e<sup>-</sup> from Ag@Fe<sub>3</sub>O<sub>4</sub> to the target, both of which contribute to achieving exceptional antibacterial and dye degradation performance.

### 3.1.6. Magnetic hysteresis loops analysis

The Vibrating Sample Magnetometer (VSM) pattern typically exhibits a hysteresis loop, illustrating the correlation between magnetic

field strength and material magnetization, thereby offering insights into the magnetic behavior of the material. The magnetization curve of the s-Fe<sub>3</sub>O<sub>4</sub> and Ag@Fe<sub>3</sub>O<sub>4</sub> particles at room temperature does not exhibit any noticeable remanence or coercivity, indicating their superparamagnetic behavior (Fig. 3e). The magnetic hysteresis loops indicate that the saturation magnetization of Ag@Fe<sub>3</sub>O<sub>4</sub> is approximately 55.5 emu g<sup>-1</sup>, which is lower than that of s-Fe<sub>3</sub>O<sub>4</sub> (72.8 emu g<sup>-1</sup>). The decrease can be attributed to the diamagnetic nature of Ag, which, when combined with the Fe<sub>3</sub>O<sub>4</sub> shell, attenuates the magnetic properties of the s-Fe<sub>3</sub>O<sub>4</sub>. Nonetheless, the Ag@Fe<sub>3</sub>O<sub>4</sub> still exhibits strong magnetic responsivity, as it has been reported that the application of a magnetic field can effectively facilitate the separation of materials from aqueous solutions when their saturation magnetization exceeds 16.3 emu·g<sup>-1</sup> (Liu et al., 2015). The strong magnetic responsivity of Ag@Fe<sub>3</sub>O<sub>4</sub> is directly demonstrated in the inset in Fig. 3e, where the particles easily attract towards an external magnetic field when a cylindrical NdFeB permanent magnet is positioned adjacent to the vial containing the Ag@Fe<sub>3</sub>O<sub>4</sub> suspension. During the process, the Ag@Fe<sub>3</sub>O<sub>4</sub> particles rapidly adhere to the inner walls of the vials within 20 s, resulting in a transparent remaining liquid.

### 3.1.7. FTIR analysis

The distinct peaks in the FTIR spectra can provide valuable information regarding the chemical composition and structure characteristic of the material. The peaks observed at approximately 594 cm<sup>-1</sup> and 429 cm<sup>-1</sup> in the Ag@Fe<sub>3</sub>O<sub>4</sub> spectrum (Fig. 3f) correspond to the stretching vibrations of the tetrahedral (Fe<sup>3+</sup>-O<sup>2-</sup>) and octahedral (Fe<sup>2+</sup>-O<sup>2-</sup>) groups, respectively, confirming the presence of Fe<sub>3</sub>O<sub>4</sub> (Husain et al., 2019). The absorption bands at around 3456 cm<sup>-1</sup> and 1632 cm<sup>-1</sup> can be attributed to vibrational peaks originating from the hydroxyl group on the surface of Ag@Fe<sub>3</sub>O<sub>4</sub>. Apart from the difference in peak intensity, the peak position of s-Fe<sub>3</sub>O<sub>4</sub> is approximately similar to that of Ag@Fe<sub>3</sub>O<sub>4</sub> due to silver's lack of absorption in the infrared region.

### 3.1.8. XPS analysis

The XPS is utilized for the validation of the electronic state and chemical composition of the particles. The XPS full spectrum of Ag@Fe<sub>3</sub>O<sub>4</sub> exhibits characteristic peaks corresponding to Fe 2p, O 1 s, and Ag 3d (Fig. S2a, Supporting Information). The peaks observed at 710.2 eV, 711.6 eV, 723.3 eV, and 725.0 eV in the Fe 2p spectrum correspond to Fe<sup>2+</sup> 2p<sub>3/2</sub>, Fe<sup>3+</sup> 2p<sub>3/2</sub>, Fe<sup>2+</sup> 2p<sub>1/2</sub> and Fe<sup>3+</sup> 2p<sub>1/2</sub>, respectively, which is in consistent with the typical peaks in Fe<sub>3</sub>O<sub>4</sub> (Fig. 3g) (Ma et al., 2015; Liang et al., 2018; Wilson and Langell, 2014; Yamashita and Hayes, 2008). The other four peaks are satellite peaks. The O 1 s spectrum can be deconvoluted into two distinct peaks, specifically at 529.8 eV (Fe-O) and 530.8 eV (H-O) (Fig. S2b, Supporting Information), which are associated with the Fe<sub>3</sub>O<sub>4</sub> and surface hydroxyl, respectively (Mu et al., 2011). The Ag 3d spectrum is deconvoluted into two distinct peaks representing Ag 3d<sub>5/2</sub> (368.0 eV) and Ag 3d<sub>3/2</sub> (374.0 eV) (Fig. 3h), which align with the established binding energy of metallic silver (Lou et al., 2013; Mottaghi et al., 2014). The XPS results prove the successful synthesis of the Ag@Fe<sub>3</sub>O<sub>4</sub> composite.

### 3.1.9. ESR analysis

The ESR technique is used to qualitatively and quantitatively detect the unpaired electrons present in atoms or molecules of materials, as well as explore the structural properties of their surroundings. The ESR patterns (Fig. 3i) demonstrate the absence of any signal peaks without light (0 min), while six characteristic peaks corresponding to superoxide radical (•O<sub>2</sub><sup>-</sup>) are observed under a mercury lamp for 2 min. The findings indicate that under light conditions, the Ag@Fe<sub>3</sub>O<sub>4</sub> exhibits oxidative properties (Lee et al., 2022; Zhao et al., 2019).

## 3.2. Antibacterial performance and its mechanism

### 3.2.1. Measurement for the diameter of inhibition zone (DIZ)

The antibacterial effectiveness of Ag@Fe<sub>3</sub>O<sub>4</sub> against *E. coli* is evaluated through the assessment for diameter of inhibition zone (DIZ), minimum inhibitory concentration (MIC), and cycling antibacterial assay. The absence of an inhibition zone around s-Fe<sub>3</sub>O<sub>4</sub> at both concentrations suggests that s-Fe<sub>3</sub>O<sub>4</sub> does not possess antibacterial properties and is incapable of forming an inhibition zone (Fig. 4a). In contrast to s-Fe<sub>3</sub>O<sub>4</sub>, both c-Ag and Ag@Fe<sub>3</sub>O<sub>4</sub> exhibit distinct inhibition zones, indicating their antibacterial properties. The DIZ of c-Ag and Ag@Fe<sub>3</sub>O<sub>4</sub> is observed to increase with their concentration, indicating a positive correlation between antibacterial activity and particle concentration. The DIZ of Ag@Fe<sub>3</sub>O<sub>4</sub> is evidently larger than that of c-Ag at equivalent concentrations, thereby indicating the superior antibacterial activity of Ag@Fe<sub>3</sub>O<sub>4</sub>. This is attributed to the tendency of c-Ag to aggregate, which results in a reduced surface area available for bacterial interaction and consequently hinders the release of silver ions responsible for antibacterial activity. In the case of Ag@Fe<sub>3</sub>O<sub>4</sub>, the porous Fe<sub>3</sub>O<sub>4</sub> shells prevent the aggregation of Ag cores and facilitate the sustained release of silver ions, thereby contributing to its superior antibacterial performance.

### 3.2.2. Measurement of the minimum inhibitory concentration (MIC)

The broth microdilution method is employed to investigate the bactericidal effect of Ag@Fe<sub>3</sub>O<sub>4</sub> at various concentrations, determining its MIC and quantitatively evaluating its efficacy against bacteria. A negative control group (only broth) and a positive control group (mixture of bacteria and broth) are set up for comparison. The bacteria

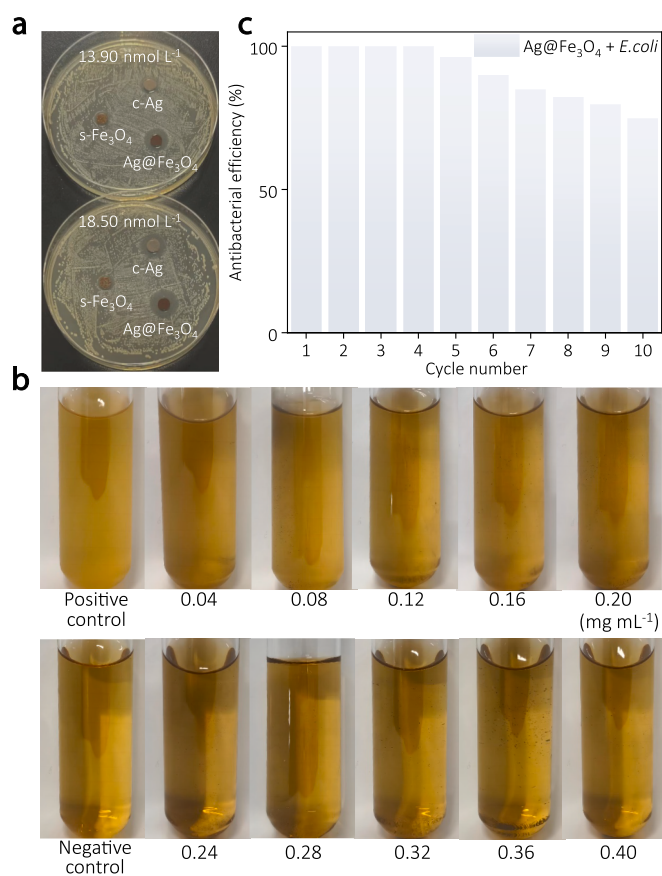


**Fig. 4.** (a) Inhibition zones of the as-synthesized c-Ag, s-Fe<sub>3</sub>O<sub>4</sub>, and Ag@Fe<sub>3</sub>O<sub>4</sub> with different concentrations against *E. coli*, (b) measurement of the minimum inhibitory concentration of the Ag@Fe<sub>3</sub>O<sub>4</sub>, (c) cycling antibacterial assessment of the Ag@Fe<sub>3</sub>O<sub>4</sub>.

continue to proliferate in the positive control group, resulting in the turbidity of the solution. The negative control group, however, exhibits a transparent solution due to the absence of bacteria (Fig. 4b). The solutions in the upper row tubes ( $0.04\text{--}0.20\text{ mg mL}^{-1}$ ) demonstrate a turbid state similar to that of the positive control group, indicating the sustained proliferation and growth of bacteria at these concentrations of the composite material. Conversely, the solutions in the lower row tubes ( $0.24\text{--}0.40\text{ mg mL}^{-1}$ ) exhibit clarity resembling that of the negative control group, thereby suggesting the inhibitory effect of the composite material on bacterial growth and reproduction at these concentrations. Consequently, the MIC for  $\text{Ag@Fe}_3\text{O}_4$  is determined as  $0.24\text{ mg mL}^{-1}$  (equivalent to  $0.042\text{ mg mL}^{-1}$  in terms of Ag), representing the lowest concentration capable of impeding bacterial growth. The low MIC indicates the superior antibacterial performance of  $\text{Ag@Fe}_3\text{O}_4$ , which can be attributed to its intricate nanostructure. The porous  $\text{Fe}_3\text{O}_4$  shell not only hinders the aggregation of Ag cores but also extends the release of silver ions, thereby contributing to an efficient and enduring antibacterial effect.

### 3.2.3. Cycling antibacterial assay

The reusability of  $\text{Ag@Fe}_3\text{O}_4$  nanocomposite is evaluated by conducting a 10-cycle antibacterial experiment against *E. coli* (Fig. 4c). The results demonstrate that the antibacterial efficacy of  $\text{Ag@Fe}_3\text{O}_4$  against *E. coli* remained stable during the first four cycles; however, it started to decline from the fifth cycle onwards, with an antibacterial efficiency of 74.6 % by the tenth cycle. This phenomenon can be attributed to the inevitable loss of  $\text{Ag@Fe}_3\text{O}_4$  over multiple cycles, which leads to a diminished inhibitory effect on bacteria. Additionally, bacterial adhesion onto the surface of the material during cycling could hinder direct contact between  $\text{Ag@Fe}_3\text{O}_4$  and bacteria, thereby reducing its effectiveness. In general, the  $\text{Ag@Fe}_3\text{O}_4$  composite exhibits exceptional cyclic antibacterial performance due to its delicate structure, in which the porous  $\text{Fe}_3\text{O}_4$  shell not only ensures sustained release of silver ions but also demonstrates excellent magnetic properties for efficient and high recovery rates under an external magnetic field.

The aforementioned advantages of  $\text{Ag@Fe}_3\text{O}_4$  function synergistically and contribute to its exceptional antibacterial performance and reutilization, surpassing that of numerous previously reported Ag-based composites (Table S2, Supporting Information), thereby demonstrating its significant potential for medical applications and sewage treatment.

### 3.2.4. Possible antibacterial mechanism

The  $\text{Ag@Fe}_3\text{O}_4$  composite demonstrates remarkable antibacterial efficacy, and multiple potential antibacterial mechanisms are implicated

(Fig. 5).

Firstly, the negatively charged bacterial cell wall strongly binds to  $\text{Ag}^+$  through Coulombic attraction. On one hand, these  $\text{Ag}^+$  impact the permeability of the bacterial membrane and disrupt both the microbial electron transport system and material transport system. On the other hand, the interaction between  $\text{Ag}^+$  and the cell wall triggers a peptidoglycan reaction, resulting in the degradation of crucial components and functional impairments within bacteria. Furthermore, penetration of  $\text{Ag}^+$  into the cell wall causes rupture and leakage of cellular fluid, ultimately resulting in bacterial death (Akhavan, 2009; Sotiriou and Pratsinis, 2010).

Secondly, upon penetration of the cell wall and entry into the bacterial cell,  $\text{Ag}^+$  selectively binds to specific groups (such as sulfhydryl group) within the bacterial cells, inducing protein coagulation. This process disrupts the enzymatic activity responsible for cellular synthesis, thereby impairing the division and reproduction ability of bacteria, ultimately leading to their demise (Yuranova et al., 2003; Ding et al., 2017).

Thirdly, the silver ions can induce DNA damage in bacteria. On one hand, silver ions can disrupt the structure and function of specific proteins, thereby reducing the efficiency of oxidative phosphorylation and impeding ATP synthesis, which results in impairment to DNA replication. On the other hand, the presence of silver ions induces the generation of reactive oxygen species (ROS, including the superoxide radical of  $\bullet\text{O}_2^-$  confirmed by the ESR analysis), which can displace hydrogen atoms within DNA molecules. This displacement results in structural deformations in bacterial DNA, thereby impeding the synthesis of DNA and proteins and ultimately rendering the bacteria inactive (Li et al., 2005; Sondi and Salopek-Sondi, 2004; Li et al., 2021; Zhang et al., 2023).

The porous  $\text{Fe}_3\text{O}_4$  shell in the  $\text{Ag@Fe}_3\text{O}_4$  effectively impedes the aggregation of Ag, ensuring a sustained release of silver ions and exhibiting exceptional magnetic properties. All these factors of  $\text{Ag@Fe}_3\text{O}_4$  function synergistically to efficiently eradicate bacteria and achieve a high recovery rate, offering great potential for the development of medical devices, antibacterial coatings, and sewage treatment applications.

### 3.3. Catalytic degradation of dyes and its mechanism

#### 3.3.1. Catalytic degradation of dyes

The as-synthesized  $\text{Ag@Fe}_3\text{O}_4$  and its control samples of c-Ag and s- $\text{Fe}_3\text{O}_4$  are subjected to the degradation experiment of organic dyes (RB, R6G, and MB) in the presence of  $\text{NaBH}_4$ . The detailed experimental

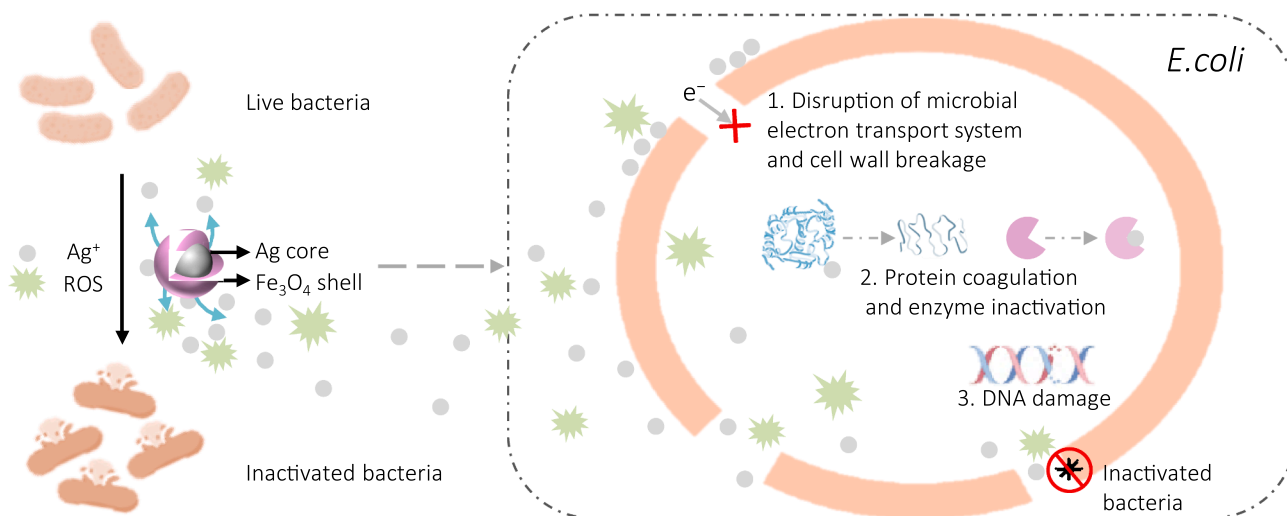


Fig. 5. The diagram illustrating the possible antibacterial mechanism of the  $\text{Ag@Fe}_3\text{O}_4$ .

parameters are as follows: the catalytic temperature is room temperature ( $\sim 25\text{ }^{\circ}\text{C}$ ), the dye concentration is  $5\text{ mg L}^{-1}$ , the solution pH is 7, and the dosage of  $\text{Ag@Fe}_3\text{O}_4$  is 20 mg per each catalytic experiment. The results indicate very little degradation of RB after 15 min by either pure  $\text{Ag@Fe}_3\text{O}_4$  (Fig. 6a) or pure  $\text{NaBH}_4$  (Fig. 6b), while the presence of both  $\text{Ag@Fe}_3\text{O}_4$  and  $\text{NaBH}_4$  achieves near complete degradation of RB within only 5 min (Fig. 6c). The corresponding digital images visually demonstrate the degradation effect of both  $\text{Ag@Fe}_3\text{O}_4$  and  $\text{NaBH}_4$  towards RB since the solution color gradually faded with the reaction time (Fig. 6d), confirming their highly efficient degradation effect. The degradation effect is further quantitatively assessed by calculating their degradation efficiency (Fig. 6e). The degradation efficiency of both  $\text{Ag@Fe}_3\text{O}_4$  and  $\text{NaBH}_4$  towards RB can reach nearly 100 % within 5 min, whereas after 15 min, the pure  $\text{Ag@Fe}_3\text{O}_4$  and pure  $\text{NaBH}_4$  only achieve approximately 18.7 % and 36.8 %, respectively. The degradation efficiency for the control samples of c-Ag and s- $\text{Fe}_3\text{O}_4$  in the presence of  $\text{NaBH}_4$  after 5 min are 48.2 % and 83.8 %, respectively, also exhibiting a limited degradation effect towards RB when compared to  $\text{Ag@Fe}_3\text{O}_4$  (Figs. S3, S4, S5, Supporting Information).

The superior degradation efficiency of  $\text{Ag@Fe}_3\text{O}_4$  towards RB can be attributed to multiple factors. Firstly, the  $\text{Fe}_3\text{O}_4$  shell effectively prevents the agglomeration of the Ag core, thereby preserving a high specific surface area and activity for the catalyst (M.a. Ghasemzadeh, J.s. Ghomi, S. Zahedi, *Fe<sub>3</sub>O<sub>4</sub> nanoparticles: A highly efficient and easily reusable catalyst for the one-pot synthesis of xanthene derivatives under solvent-free conditions*, *Journal of the Serbian Chemical Society* 78(6), 2013; Wang et al., 2021). Secondly, the presence of mesopores and abundant active sites in the  $\text{Fe}_3\text{O}_4$  shell enhances dye adsorption efficiency and facilitates increased contact between dye molecules and Ag core. Thirdly, the Ag with high electrical conductivity serves as an electron mediator, capturing electrons from the nucleophilic  $\text{NaBH}_4$  and transferring them to the electrophilic RB during the reaction, ultimately resulting in efficient degradation of the RB (ZhongJie Jiang, 2005; Zheng and Wang, 2012). The degradation performance of RB by  $\text{Ag@Fe}_3\text{O}_4$  surpasses that of pure c-Ag and s- $\text{Fe}_3\text{O}_4$ , owing to the synergistic effect resulting from the aforementioned advantages of  $\text{Fe}_3\text{O}_4$

shell and Ag core.

Similarly, the  $\text{Ag@Fe}_3\text{O}_4$  demonstrates remarkable degradation efficiency towards various organic dyes, including R6G (Fig. 7) and MB (Fig. 8). The  $\text{Ag@Fe}_3\text{O}_4$  can completely degrade R6G within 5 min in the presence of  $\text{NaBH}_4$ , outperforming the control samples of pure  $\text{Ag@Fe}_3\text{O}_4$  and pure  $\text{NaBH}_4$ , as evidenced by the UV-vis spectra and corresponding digital images (Fig. 7).

The  $\text{Ag@Fe}_3\text{O}_4$  also exhibit the superior degradation performance towards MB (Fig. 8). The remarkable degradation capability of  $\text{Ag@Fe}_3\text{O}_4$  towards RB, R6G, and MB proves its relatively universal effect on degrading organic dyes, thereby indicating its potential for practical application in dye-containing wastewater treatment.

### 3.3.2. Cycling degradation property

To assess the practical applicability of  $\text{Ag@Fe}_3\text{O}_4$  in wastewater treatment, the investigation into its cycling degradation property is conducted. During the experiment,  $\text{Ag@Fe}_3\text{O}_4$  is easily reused by being collected with a magnet. The results demonstrate that even after 6 consecutive cycles of reutilization, the  $\text{Ag@Fe}_3\text{O}_4$  still exhibits a remarkable degradation efficiency of 90.9 % towards RB, highlighting its exceptional potential for practical wastewater treatment (Fig. 9a). Similarly, the  $\text{Ag@Fe}_3\text{O}_4$  exhibit excellent catalytic degradation efficiency towards Rhodamine 6G (Fig. 9b) and Methylene blue (Fig. 9c) after 6 cycles, both of which achieving 100 %.

The decrease in the degradation efficiency of  $\text{Ag@Fe}_3\text{O}_4$  towards organic dyes with increasing cycle number may be attributed to several factors. Firstly, during the process of magnetic recovery, some loss of  $\text{Ag@Fe}_3\text{O}_4$  nanoparticles is inevitable (such as incomplete separation of nanoparticles from the solution and adherence of particles to container surfaces), leading to a reduction in degradation efficiency during subsequent cycles due to the decrease in available catalyst. Secondly, during cycling, the surface of  $\text{Ag@Fe}_3\text{O}_4$  nanoparticles can become fouled with reaction intermediates, by-products, or residual organic dyes, thereby obstructing active sites on the nanoparticles and diminishing their catalytic efficiency. Thirdly, the leaching and loss of the silver component in  $\text{Ag@Fe}_3\text{O}_4$  during the degradation process can result in a reduction of

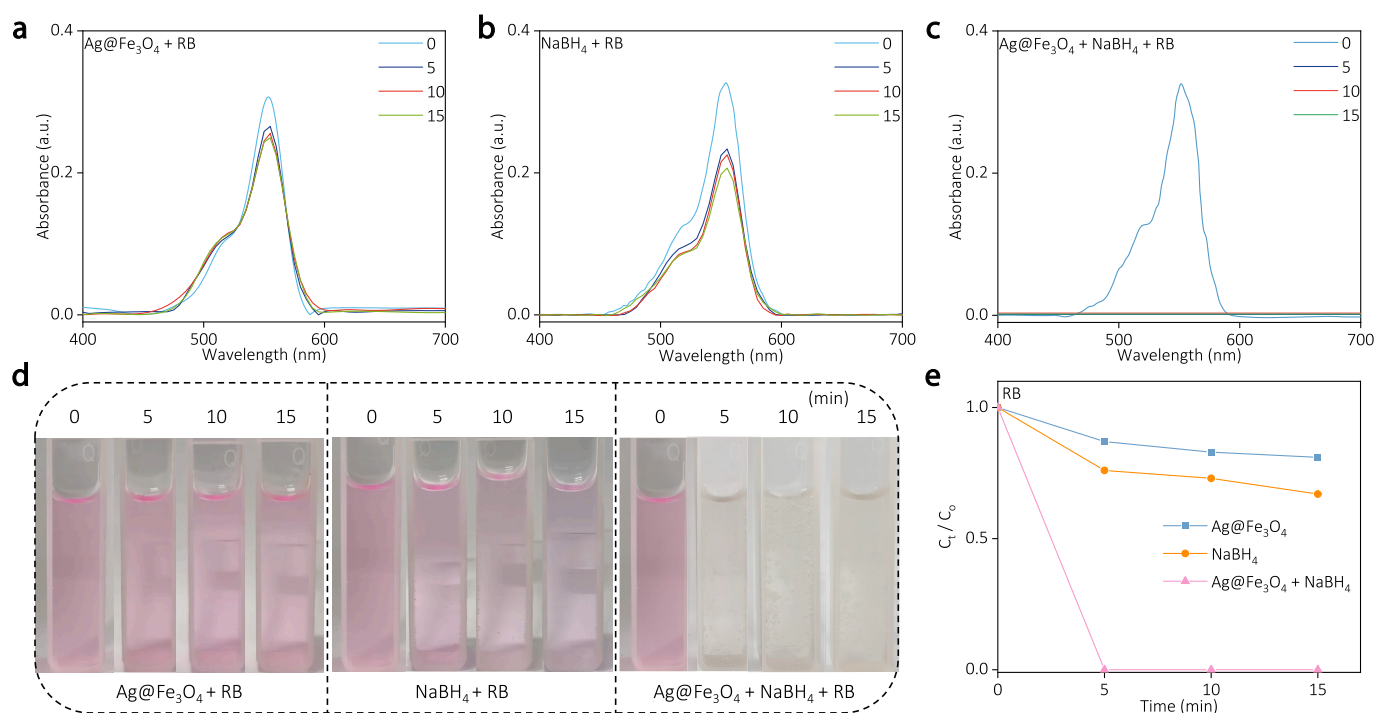


**Fig. 6.** The degradation of RB by pure  $\text{Ag@Fe}_3\text{O}_4$ , pure  $\text{NaBH}_4$ , and “ $\text{Ag@Fe}_3\text{O}_4 + \text{NaBH}_4$ ”: (a-c) the UV-vis spectra at different time, (d) corresponding digital images, and (e) degradation efficiency over time.

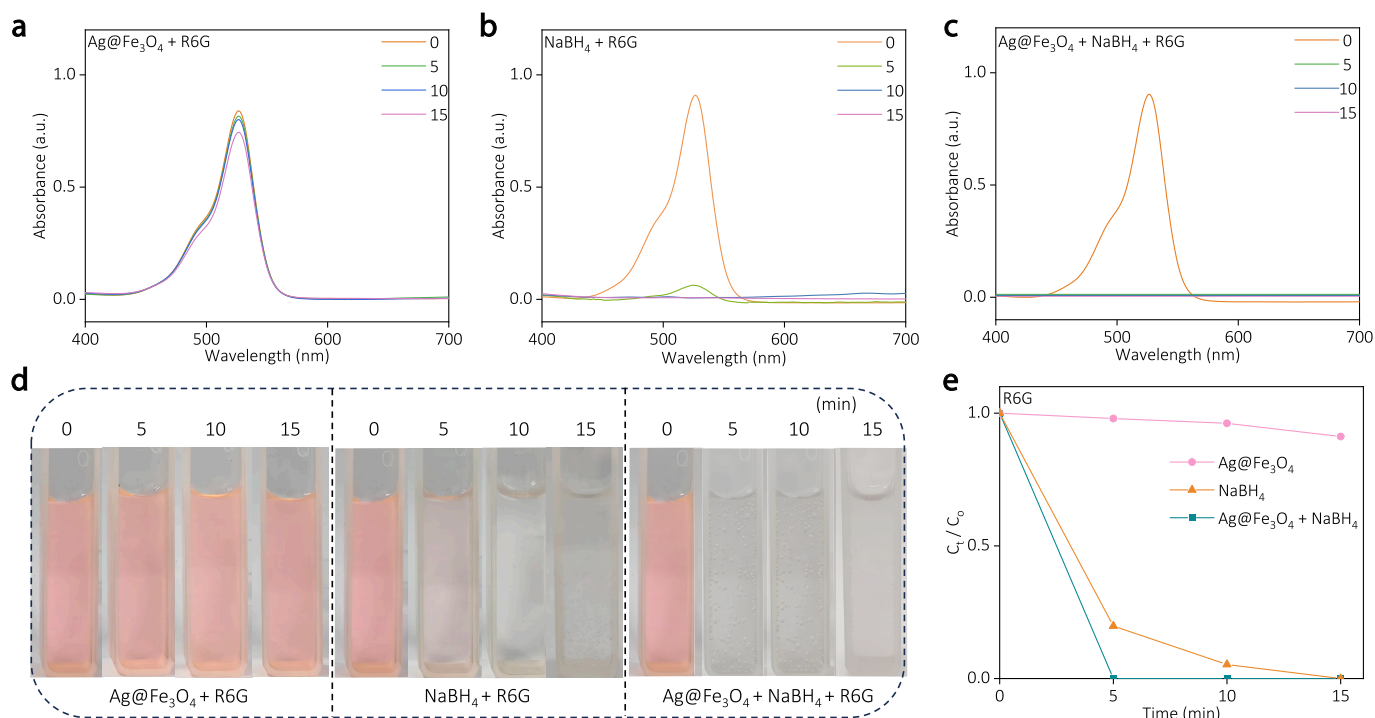


**Fig. 7.** The degradation of R6G by pure Ag@Fe<sub>3</sub>O<sub>4</sub>, pure NaBH<sub>4</sub>, and “Ag@Fe<sub>3</sub>O<sub>4</sub> + NaBH<sub>4</sub>”: (a-c) the UV-vis spectra at different time, (d) corresponding digital images, and (e) degradation efficiency over time.

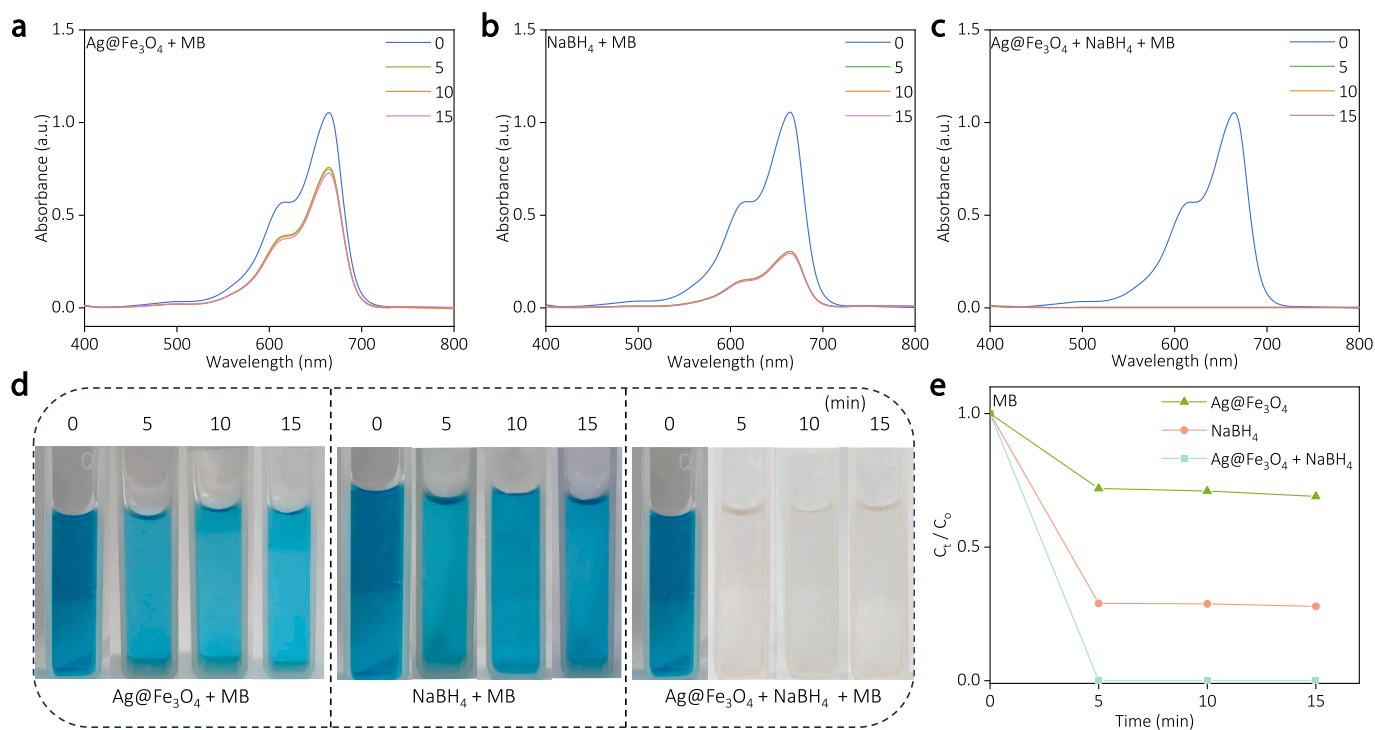


**Fig. 8.** The degradation of MB by pure Ag@Fe<sub>3</sub>O<sub>4</sub>, pure NaBH<sub>4</sub>, and “Ag@Fe<sub>3</sub>O<sub>4</sub> + NaBH<sub>4</sub>”: (a-c) the UV-vis spectra at different time, (d) corresponding digital images, and (e) degradation efficiency over time.

catalytic activity, as silver plays a crucial role in the degradation mechanism (Wang et al., 2021).

Despite a decrease in degradation efficiency with an increasing cycle number, the overall degradation efficiency of RB, R6G, and MB can still exceed 90.9 % after 6 cycles, highlighting the superior degradation efficiency of Ag@Fe<sub>3</sub>O<sub>4</sub> towards organic dyes. The catalytic degradation

efficiency of the obtained Ag@Fe<sub>3</sub>O<sub>4</sub> towards various organic dyes surpasses that of many previously reported Ag-based composites (Table S3, Supporting Information). Additionally, the Ag@Fe<sub>3</sub>O<sub>4</sub> is cost-effective (around \$0.17 per gram in terms of chemical reagents, the detailed calculation can be seen in Table S4, Supporting Information), underscoring its potential for practical applications in dye-containing

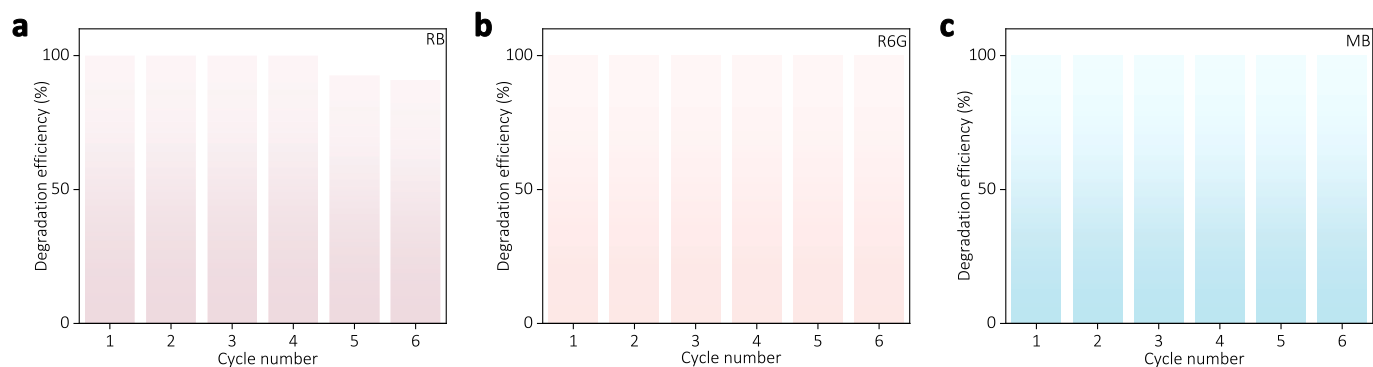


Fig. 9. Cycling degradation performance of the Ag@Fe<sub>3</sub>O<sub>4</sub> towards (a) RB, (b) R6G, and (c) MB.

wastewater treatment.

### 3.3.3. Possible degradation mechanism

The Ag@Fe<sub>3</sub>O<sub>4</sub> exhibit exceptional catalytic degradation properties towards organic dyes, involving multiple potential mechanisms. The degradation of RB can be taken as an example (Figure S6, Supporting Information). The cationic dye RB is electrostatically attracted to the hydroxyl groups on the surface of the Fe<sub>3</sub>O<sub>4</sub> shell or adsorbed onto the active sites on the Fe<sub>3</sub>O<sub>4</sub> shell through van der Waals force. The Ag serves as an electron transfer mediator, facilitating the efficient electron transfer from the nucleophilic NaBH<sub>4</sub> to the electrophilic RB molecules. The electrons induce reduction of the chromophoric structure and disruption of the conjugated system in RB, leading to the decoloration of the dye. The final products may consist of Leuco-Rhodamine B, aminated and de-ethylated derivatives, as well as inorganic byproducts (potentially including borates) (Liu et al., 2023; Wang et al., 2016). The degradation process of R6G (Fig. S7, Supporting Information) and MB (Fig. S8, Supporting Information) is similar to that of RB, except for the potential final products differing from each other.

## 4. Conclusions

The magnetoplasmonic core-shell structured Ag@Fe<sub>3</sub>O<sub>4</sub> particles have been synthesized via a one-step polyol reduction process, exhibiting dual functionality for bacteria eradication and organic dyes degradation. The delicate nanostructure of the Ag@Fe<sub>3</sub>O<sub>4</sub> not only enhances the antibacterial efficacy and catalytic degradation efficiency of the particles but also exploits the magnetic properties of Fe<sub>3</sub>O<sub>4</sub> for facile recovery and reutilization. The Ag@Fe<sub>3</sub>O<sub>4</sub> exhibits nearly 100 % inhibition of *E. coli* at a concentration of 0.24 mg mL<sup>-1</sup> (with an Ag content of 0.042 mg mL<sup>-1</sup>), while maintaining antibacterial efficacy at 74.6 % even after undergoing reutilization for 10 cycles. Meanwhile, the Ag@Fe<sub>3</sub>O<sub>4</sub> exhibits remarkable efficacy in catalytically degrading various organic dyes (including Rhodamine B, Rhodamine 6G, and Methylene blue) within only 15 min in the presence of NaBH<sub>4</sub>, while achieving an impressive degradation efficiency exceeding 90.9 % after undergoing 6 cycles. The cost-effectiveness (approximately \$0.17 per gram) and facile magnetic recovery of Ag@Fe<sub>3</sub>O<sub>4</sub> particles further augment their practicality for large-scale applications in antibacterial treatments and environmental remediation, thereby promoting both ecological conservation and efficient resource utilization. The future research could focus on optimizing the synthesis parameters and scalability of the production process, functionalizing the surface with specific ligands or coatings to enhance interaction with target molecules or bacteria, combining Ag@Fe<sub>3</sub>O<sub>4</sub> with other nanomaterials to create hybrid systems that offer synergistic effects, and integrating the nanoparticles into practical devices or systems for antibacterial applications and water purification (such as filters, coatings, and sensors).

## CRedit authorship contribution statement

**Qing Shen:** Writing – original draft, Formal analysis, Data curation. **Luping Zhang:** Writing – review & editing. **Yuan Zhao:** Writing – review & editing. **Xiaobing Han:** Writing – review & editing. **Jie Gao:** Writing – review & editing. **Yuesheng Li:** Writing – review & editing. **Xiaoming Zhu:** Writing – review & editing. **Tian Liang:** Writing – review & editing, Formal analysis, Conceptualization. **Tao Chen:** Writing – review & editing.

## Declaration of Competing Interest

The authors declare that they have no known competing financial interests or personal relationships that could have appeared to influence the work reported in this paper.

## Acknowledgments

This work was financially supported by the Scientific Research Foundation of Hubei University of Science and Technology, China (2022ZX10, BK202314, 2022T03).

## Appendix A. Supplementary data

Supplementary data to this article can be found online at <https://doi.org/10.1016/j.arabjc.2024.106058>.

## References

- Akhavan, O., 2009. Lasting antibacterial activities of Ag-TiO<sub>2</sub>/Ag/a-TiO<sub>2</sub> nanocomposite thin film photocatalysts under solar light irradiation. *J. Colloid Interface Sci.* 336 (1), 117–124. <https://doi.org/10.1016/j.jcis.2009.03.018>.
- Aldosari, B.N., Abd El-Aal, M., Abo Zeid, E.F., Faris, T.M., Aboelela, A., Abdellatif, A.A. H., Tawfeek, H.M., 2023. Synthesis and characterization of magnetic Ag-Fe<sub>3</sub>O<sub>4</sub>@ polymer hybrid nanocomposite systems with promising antibacterial application. *Drug Dev. Ind. Pharm.* 49 (12), 723–733. <https://doi.org/10.1080/03639045.2023.2277812>.
- Amir, M., Kurtan, U., Baykal, A., 2015. Rapid color degradation of organic dyes by Fe<sub>3</sub>O<sub>4</sub>@His@Ag recyclable magnetic nanocatalyst. *J. Ind. Eng. Chem.* 27, 347–353. <https://doi.org/10.1016/j.jiec.2015.01.013>.
- Anandan, S., Grieser, F., Ashokkumar, M., 2008. Sonochemical synthesis of Au-Ag core-shell bimetallic nanoparticles. *J. Phys. Chem. C* 112 (39), 15102–15105. <https://doi.org/10.1021/jp806960r>.
- Berger, T.J., Spadaro, J.A., Bierman, R., Chapin, S.E., Becker, R.O., 1976. Antifungal properties of electrically generated metallic ions. *American Society for Microbiology* 10 (5), 856–860. <https://doi.org/10.1128/aac.10.5.856>.
- Brollo, M.E.N.F., RomanLopez-Ruiz, D., Muraca, S.J.A., Figueroa, K.R., Pirola, M Knobel, 2014. Compact Ag@Fe<sub>3</sub>O<sub>4</sub> Core-shell nanoparticles by means of single-step thermal decomposition reaction. *Sci. Rep.* 4 (1), 6839. <https://doi.org/10.1038/srep06839>.
- Chaukura, N., Gwenzi, W., Bunhu, T., Ruziwa, D.T., Pumure, I., 2016. Potential uses and value-added products derived from waste polystyrene in developing countries: A review. *Resour. Conserv. Recycl.* 107, 157–165. <https://doi.org/10.1016/j.resconrec.2015.10.031>.
- Chen, B., Jiao, X., Chen, D., 2010. Size-Controlled and Size-Designed Synthesis of Nano Submicrometer Ag Particles. *Cryst. Growth Des.* 10 (8), 3378–3386. <https://doi.org/10.1021/cg901497p>.

- Chen, Y., Wu, J., Hu, Z., Zhou, D., Xie, H., Dong, C., 2014. Amorphous InGaZnO Thin Film Transistors with Wet-Etched Ag Electrodes. *ECS Solid State Lett.* 3 (6), Q29–Q32. <https://doi.org/10.1149/2.001406ssl>.
- Cinteza, L.O., Scormorocco, C., Voicu, S.N., Nistor, C.L., Nitu, S.G., Trica, B., Jecu, M. L., Petcu, C., 2018. Chitosan-stabilized Ag nanoparticles with superior biocompatibility and their synergistic antibacterial effect in mixtures with essential oils. *Nanomaterials* 8 (10), 826. <https://doi.org/10.3390/nano8100826>.
- Ding, X., Yuan, P., Gao, N., Zhu, H., Yang, Y.Y., Xu, Q.-H., 2017. Au-Ag core-shell nanoparticles for simultaneous bacterial imaging and synergistic antibacterial activity. *Nanomedicine: Nanotechnology, Biology and Medicine* 13 (1), 297–305. <https://doi.org/10.1016/j.nano.2016.09.003>.
- Dong, Y.X., Jin, B., Lee, S.H., Wang, X.L., Jin, E.M., Jeong, S.M., 2019. One-step hydrothermal synthesis of Ag decorated TiO<sub>2</sub> nanoparticles for dye-sensitized solar cell application. *Renew. Energy* 135, 1207–1212. <https://doi.org/10.1016/j.renene.2018.12.062>.
- Fouladi-Fard, R., Aali, R., Mohammadi-Aghdam, S., Mortazavi-derazkola, S., 2022. The surface modification of spherical ZnO with Ag nanoparticles: A novel agent, biogenic synthesis, catalytic and antibacterial activities. *Arab. J. Chem.* 15 (3), 103658. <https://doi.org/10.1016/j.arabj.2021.103658>.
- Gankhuyag, S., Bae, D.S., Lee, K., Lee, S., 2021. One-Pot Synthesis of SiO<sub>2</sub>@Ag Mesoporous Nanoparticle Coating for Inhibition of Escherichia coli Bacteria on Various Surfaces. *Nanomaterials* 11 (2), 549. <https://doi.org/10.3390/nano11020549>.
- Ghasemzadeh, M.A., Ghomi, J.S., Zahedi, S., 2013. Fe<sub>3</sub>O<sub>4</sub> nanoparticles: A highly efficient and easily reusable catalyst for the one-pot synthesis of xanthene derivatives under solvent-free conditions. *J. Serbian Chem. Soc.* 78 (6), 769–779. <https://doi.org/10.2298/jsc120624156g>.
- Ghosh, M., Mondal, M., Mandal, S., Roy, A., Chakrabarty, S., Chakrabarti, G., Pradhan, S. K., 2020. Enhanced photocatalytic and antibacterial activities of mechanosynthesized TiO<sub>2</sub>-Ag nanocomposite in wastewater treatment. *J. Mol. Struct.* 1211, 128076. <https://doi.org/10.1016/j.molstruc.2020.128076>.
- Gong, P., Li, H., He, X., Wang, K., Hu, J., Tan, W., Zhang, S., Yang, X., 2007. Preparation and antibacterial activity of Fe<sub>3</sub>O<sub>4</sub>@Ag nanoparticles. *Nanotechnology* 18 (28), 285604. <https://doi.org/10.1088/0957-4484/18/28/285604>.
- Hao, X., Zhao, J., Zhao, Y., Ma, D., Lu, Y., Guo, J., Zeng, Q., 2013. Mild aqueous synthesis of urchin-like MnOx hollow nanostructures and their properties for RhB degradation. *Chem. Eng. J.* 229, 134–143. <https://doi.org/10.1016/j.cej.2013.06.007>.
- Height, M.J., Pratsinis, S.E., Mekasuwandromong, O., Praserthdam, P., 2006. Ag-ZnO catalysts for UV-photodegradation of methylene blue. *Appl Catal B* 63 (3–4), 305–312. <https://doi.org/10.1016/j.apcatb.2005.10.018>.
- Hou, Y., Yuan, H., Chen, H., Shen, J., Li, L., 2017. The preparation and lithium battery performance of core-shell SiO<sub>2</sub>@Fe<sub>3</sub>O<sub>4</sub>@C composite. *Ceram. Int.* 43 (14), 11505–11510. <https://doi.org/10.1016/j.ceramint.2017.05.357>.
- Husain, S., Irfansyah, M., Haryanti, N.H., Suryajaya, S., Arjo, S., Maddu, A., 2019. Synthesis and characterization of Fe<sub>3</sub>O<sub>4</sub> magnetic nanoparticles from iron ore. *J. Phys. Conf. Ser.* 1242 (1), 012021. <https://doi.org/10.1088/1742-6596/1242/1/012021>.
- Islam, M.A., Jacob, M.V., Antunes, E., 2021. A critical review on silver nanoparticles: From synthesis and applications to its mitigation through low-cost adsorption by biochar. *J. Environ. Manage.* 281, 111918. <https://doi.org/10.1016/j.jenvman.2020.111918>.
- Jeon, H., Yi, S., Oh, S., 2003. Preparation and antibacterial effects of Ag-SiO<sub>2</sub> thin films by sol-gel method. *Biomaterials* 24 (27), 4921–4928. [https://doi.org/10.1016/S0142-9612\(03\)00415-0](https://doi.org/10.1016/S0142-9612(03)00415-0).
- Jia, L., Qiu, S., Sun, Y., Song, H., Hao, R., 2017. Stable nanocomposite based on PEGylated and silver nanoparticles loaded graphene oxide for long-term antibacterial activity. *ACS Appl. Mater. Interfaces* 9 (18), 15328–15341. <https://doi.org/10.1021/acsami.7b03987>.
- Jiao, Y., Wan, C., Bao, W., Gao, H., Liang, D., Li, J., 2018. Facile hydrothermal synthesis of Fe<sub>3</sub>O<sub>4</sub>@cellulose aerogel nanocomposite and its application in Fenton-like degradation of Rhodamine B. *Carbohydr. Polym.* 189, 371–378. <https://doi.org/10.1016/j.carbpol.2018.02.028>.
- Jie Jiang, Z., Liu, C., Sun, L., 2005. Catalytic properties of silver nanoparticles supported on silica spheres. *J. Phys. Chem. B* 109 (5), 1730–1735. <https://doi.org/10.1021/jp046032g>.
- Joshi, P., Zhou, Y., Ahmadov, T.O., Zhang, P., 2014. Quantitative SERS-based detection using Ag-Fe<sub>3</sub>O<sub>4</sub> nanocomposites with an internal reference. *J. Mater. Chem. C* 2 (46), 9964–9968. <https://doi.org/10.1039/C4TC01550A>.
- Lee, D.-E., Devthade, V., Moru, S., Jo, W.-K., Tonda, S., 2022. Magnetically sensitive TiO<sub>2</sub> hollow sphere/Fe<sub>3</sub>O<sub>4</sub> core-shell hybrid catalyst for high-performance sunlight-assisted photocatalytic degradation of aqueous antibiotic pollutants. *J. Alloy. Compd.* 902, 163612. <https://doi.org/10.1016/j.jallcom.2022.163612>.
- Li, P., Li, J., Wu, C., Wu, Q., Li, J., 2005. Synergistic antibacterial effects of β-lactam antibiotic combined with silver nanoparticles. *Nanotechnology* 16 (9), 1912–1917. <https://doi.org/10.1088/0957-4484/16/9/082>.
- Li, P., Wu, H., Dong, A., 2021. Ag/AgX nanostructures serving as antibacterial agents: achievements and challenges. *Rare Met.* 41 (2), 519–539. <https://doi.org/10.1007/s12598-021-01822-0>.
- Liang, T., Wang, H., Xu, D., Liao, K., Wang, R., He, B., Gong, Y., Yan, C., 2018. High-energy flexible quasi-solid-state lithium-ion capacitors enabled by a freestanding rGO-encapsulated Fe<sub>3</sub>O<sub>4</sub> nanocube anode and a holey rGO film cathode. *Nanoscale* 10 (37), 17814–17823. <https://doi.org/10.1039/c8nr04292f>.
- Liang, T., Li, Z., Bai, Y., Yin, Y., 2023. Dichroic switching of core-shell plasmonic nanoparticles on reflective surfaces. *Exploration* 20210234. <https://doi.org/10.1002/exp.20210234>.
- Liu, G., Wang, N., Zhou, J., Wang, A., Wang, J., Jin, R., Lv, H., 2015. Microbial preparation of magnetite reduced graphene oxide nanocomposites for the removal of organic dyes from aqueous solutions. *RSC Adv.* 5 (116), 95857–95865. <https://doi.org/10.1039/c5ra18136d>.
- Liu, M., Ye, Y., Ye, J., Gao, T., Wang, D., Chen, G., Song, Z., 2023. Recent advances of magnetite (Fe<sub>3</sub>O<sub>4</sub>)-based magnetic materials in catalytic applications. *Magnetochemistry* 9 (4), 110. <https://doi.org/10.3390/magnetochemistry9040110>.
- Lou, Z., Huang, B., Wang, Z., Zhang, R., Yang, Y., Qin, X., Zhang, X., Dai, Y., 2013. Fast-generation of Ag<sub>3</sub>PO<sub>4</sub> concave microcrystals from electrochemical oxidation of bulk silver sheet. *CrystEngComm* 15 (25), 5070–5075. <https://doi.org/10.1039/c3ce40333e>.
- Lu, X., Au, L., McLellan, J., Li, Z., Marquez, M., Xia, Y., 2007. Fabrication of cubic nanocages and nanoframes by dealloying Au/Ag alloy nanoboxes with an aqueous etchant based on Fe(NO<sub>3</sub>)<sub>3</sub> or NH<sub>4</sub>OH. *Nano Lett.* 7 (6), 1764–1769. <https://doi.org/10.1021/nl070838l>.
- Ma, J., Wang, K., Zhan, M., 2015. Growth Mechanism and Electrical and Magnetic Properties of Ag-Fe<sub>3</sub>O<sub>4</sub> Core-Shell Nanowires. *ACS Appl. Mater. Interfaces* 7 (29), 16027–16039. <https://doi.org/10.1021/acsami.5b04342>.
- Mei, L., Lu, Z., Zhang, X., Li, C., Jia, Y., 2014. Polymer-Ag Nanocomposites with Enhanced Antimicrobial Activity against Bacterial Infection. *ACS Appl. Mater. Interfaces* 6 (18), 15813–15821. <https://doi.org/10.1021/am502886m>.
- Mohajeri, A., Burnett, L., Smith, J.V., Kurmus, H., Milas, J., Arulrajah, A., Horpibulsuk, S., Kadir, A.A., 2019. Nanoparticles in construction materials and other applications and implications of nanoparticle use. *Materials* 12 (19), 3052. <https://doi.org/10.3390/ma12193052>.
- Mottaghi, N., Ranjbar, M., Farrokhpour, H., Khoshouei, M., Khoshouei, A., Kameli, P., Salamati, H., Tabrizchi, M., Jalilian-Nosrati, M., 2014. Ag/Pd core-shell nanoparticles by a successive method: Pulsed laser ablation of Ag in water and reduction reaction of PdCl<sub>2</sub>. *Appl. Surf. Sci.* 292, 892–897. <https://doi.org/10.1016/j.apsusc.2013.12.075>.
- Mu, J., Chen, B., Guo, Z., Zhang, M., Zhang, Z., Zhang, P., Shao, C., Liu, Y., 2011. Highly dispersed Fe<sub>3</sub>O<sub>4</sub> nanosheets on one-dimensional carbon nanofibers: Synthesis, formation mechanism, and electrochemical performance as supercapacitor electrode materials. *Nanoscale* 3 (12), 5034–5040. <https://doi.org/10.1039/c1nr10972c>.
- Parvekar, P., Palaskar, J., Metgud, S., Maria, R., Dutta, S., 2020. The minimum inhibitory concentration (MIC) and minimum bactericidal concentration (MBC) of silver nanoparticles against Staphylococcus aureus. *Biomater. Invest. Dent.* 7 (1), 105–109. <https://doi.org/10.1080/26415275.2020.1796674>.
- Rajesh, C.S.S.D., 2012. Briefly brominated Ag thin films: XRD, FESEM, and optical studies of surface modification. *Appl. Surf. Sci.* 259, 276–282. <https://doi.org/10.1016/j.apsusc.2012.07.032>.
- Razavi, R., Amiri, M., Alshamsi, H.A., Eslaminejad, T., Salavati-Niasari, M., 2021. Green synthesis of Ag nanoparticles in oil-in-water nano-emulsion and evaluation of their antibacterial and cytotoxic properties as well as molecular docking. *Arab. J. Chem.* 14 (9), 103323. <https://doi.org/10.1016/j.arabj.2021.103323>.
- Sakir, M., Onses, M.S., 2019. Solid substrates decorated with Ag nanostructures for the catalytic degradation of methyl orange. *Results Phys.* 12, 1133–1141. <https://doi.org/10.1016/j.rinp.2018.12.084>.
- Salam, M.A., Al-Amin, M.Y., Salam, M.T., Pawar, J.S., Akhter, N., Rabaan, A.A., Alqumber, M.A.A., 2023. Antimicrobial Resistance: A Growing Serious Threat for Global Public Health. *Healthcare* 11 (13), 1946. <https://doi.org/10.3390/healthcare11131946>.
- Shakoori, A.R., Muneer, B., 2002. Copper-Resistant Bacteria from Industrial Effluents and Their Role in Remediation of Heavy Metals in Wastewater. *Folia Microbiol.* 47, 43–50. <https://doi.org/10.1007/BF02818564>.
- Sheng, Y., Xue, J., 2012. Synthesis and properties of Au-Fe<sub>3</sub>O<sub>4</sub> heterostructured nanoparticles. *J. Colloid Interface Sci.* 374 (1), 96–101. <https://doi.org/10.1016/j.jcis.2012.01.034>.
- Shi, X., Huang, C., Zheng, Z., Zhong, B., Ding, G., Li, J., You, L., Wang, S., 2021. Preparation of Magnetically Recoverable MPTIP-Ag Composite Nanoparticles and Their Application as High-Performance Catalysts. *Langmuir* 37 (34), 10249–10258. <https://doi.org/10.1021/acs.langmuir.1c00944>.
- Shrivastava, K.C., Pandey, A.K., Chappa, S., Srivastava, A.P., Sen, D., Sahu, A.K., 2022. Study on formation of Pd nanocatalyst in self-reducing silica nanotube produced by using sacrificial Fe<sub>3</sub>O<sub>4</sub> template and its efficacy in Cr(VI) reduction. *Mater. Chem. Phys.* 278, 125580. <https://doi.org/10.1016/j.matchemphys.2021.125580>.
- Shuai, C., Liu, G., Yang, Y., Qi, F., Peng, S., Yang, W., He, C., Wang, G., Qian, G., 2020. A strawberry-like Ag-decorated barium titanate enhances piezoelectric and antibacterial activities of polymer scaffold. *Nano Energy* 74, 104852. <https://doi.org/10.1016/j.nanoen.2020.104852>.
- I. Sondi, B. Salopek-Sondi, Silver nanoparticles as antimicrobial agent: a case study on E. coli as a model for Gram-negative bacteria, *Journal of Colloid and Interface Science* 275(1) (2004) 177-182. DOI: 10.1016/j.jcis.2004.02.012.
- Sotiriou, G.A., Pratsinis, S.E., 2010. Antibacterial activity of nanosilver ions and particles. *Environ. Sci. Tech.* 44 (14), 5649–5654. <https://doi.org/10.1021/es101072s>.
- Tang, S., Zheng, J., 2018. Antibacterial Activity of Silver Nanoparticles: Structural Effects. *Adv. Healthc. Mater.* 7 (13), 1701503. <https://doi.org/10.1002/adhm.201701503>.
- Tayyaba, Rehman, F.U., Shaikh, S., Tanziela, Semcheddine, F., Du, T., Jiang, H., Wang, X., 2020. In situ self-assembled Ag-Fe<sub>3</sub>O<sub>4</sub> nanoclusters in exosomes for cancer diagnosis. *J. Mater. Chem. B* 8 (14), 2845–2855. <https://doi.org/10.1039/c9tb02610j>.
- Vijayakumar, R., Koltypin, Y., Felner, I., Gedanken, A., n.d. Sonochemical synthesis and characterization of pure nanometer-sized Fe<sub>3</sub>O<sub>4</sub> particles. *Mat. Sci. Eng. A* 286 (1), 101–105. [https://doi.org/10.1016/S0921-5093\(00\)00647-X](https://doi.org/10.1016/S0921-5093(00)00647-X).

- Wang, G., Chen, Z., Chen, T., Lv, K., Reheman, A., Hu, J., 2021. Rhodium nanoparticles supported on 2-(aminomethyl) phenols-modified Fe<sub>3</sub>O<sub>4</sub> spheres as a magnetically recoverable catalyst for reduction of nitroarenes and the degradation of dyes in water. *Catal. Lett.* 152 (4), 1076–1085. <https://doi.org/10.1007/s10562-021-03688-4>.
- Wang, P., Wang, X., Yu, S., Zou, Y., Wang, J., Chen, Z., Alharbi, N.S., Alsaedi, A., Hayat, T., Chen, Y., Wang, X., 2016. Silica coated Fe<sub>3</sub>O<sub>4</sub> magnetic nanospheres for high removal of organic pollutants from wastewater. *Chem. Eng. J.* 306, 280–288. <https://doi.org/10.1016/j.cej.2016.07.068>.
- Wang, K., Zhan, S., Sun, H., Zhang, D., Wang, J., 2020. Hollow porous core-shell ZnFe<sub>2</sub>O<sub>4</sub>/AgCl nanocubes coated with EDTA and Ag nanoparticles for enhanced photocatalytic performances of visible-light-driven. *Chem. Eng. J.* 400, 125908. <https://doi.org/10.1016/j.cej.2020.125908>.
- Wei, Y., Han, B., Hu, X., Lin, Y., Wang, X., Deng, X., 2012. Synthesis of Fe<sub>3</sub>O<sub>4</sub> nanoparticles and their magnetic properties. *Procedia Eng.* 27, 632–637. <https://doi.org/10.1016/j.proeng.2011.12.498>.
- Wilson, D., Langell, M.A., 2014. XPS analysis of oleylamine/oleic acid capped Fe<sub>3</sub>O<sub>4</sub> nanoparticles as a function of temperature. *Appl. Surf. Sci.* 303, 6–13. <https://doi.org/10.1016/j.apsusc.2014.02.006>.
- X.h. Meng, X. Shao, H.y. Li, F.z. Liu, X.p. Pu, W.z. Li, C.h. Su, One-step hydrothermal synthesis, characterization and visible-light catalytic property of Ag-reduced graphene oxide composite, *Materials Research Bulletin* 48(4) (2013) 1453-1457. DOI: DOI: 10.1016/j.materresbull.2012.12.037.
- Xiong, R., Lu, C., Wang, Y., Zhou, Z., Zhang, X., 2013. Nanofibrillated cellulose as the support and reductant for the facile synthesis of Fe<sub>3</sub>O<sub>4</sub>/Ag nanocomposites with catalytic and antibacterial activity. *J. Mater. Chem. A* 1 (47). <https://doi.org/10.1039/c3ta13314a>.
- Yamashita, T., Hayes, P., 2008. Analysis of XPS spectra of Fe<sup>2+</sup> and Fe<sup>3+</sup> ions in oxide materials. *Appl. Surf. Sci.* 254 (8), 2441–2449. <https://doi.org/10.1016/j.apsusc.2007.09.063>.
- Yang, Y., Wu, X., He, C., Huang, J., Yin, S., Zhou, M., Ma, L., Zhao, W., Qiu, L., Cheng, C., 2020. Metal-organic framework Ag-based hybrid nanoagents for rapid and synergistic bacterial eradication. *ACS Appl. Mater. Interfaces* 12 (12), 13698–13708. <https://doi.org/10.1021/acsami.0c01666>.
- Ye, H., Cheng, J., Yu, K., 2019. In situ reduction of silver nanoparticles by gelatin to obtain porous silver nanoparticle chitosan composites with enhanced antimicrobial and wound-healing activity. *Int. J. Biol. Macromol.* 121, 633–642. <https://doi.org/10.1016/j.ijbiomac.2018.10.056>.
- Yong, C., Chen, X., Xiang, Q., Li, Q., Xing, X., 2018. Recyclable magnetite-silver heterodimer nanocomposites with durable antibacterial performance. *Bioact. Mater.* 3 (1), 80–86. <https://doi.org/10.1016/j.bioactmat.2017.05.008>.
- Yu, Y., Li, Y., Wang, Y., Zou, B., 2018. Self-template etching synthesis of urchin-like Fe<sub>3</sub>O<sub>4</sub> microspheres for enhanced heavy metal ions removal. *Langmuir* 34 (32), 9359–9365. <https://doi.org/10.1021/acs.langmuir.8b01219>.
- Yuranova, T., Rincon, A.G., Bozzi, A., Parra, S., Pulgarin, C., Albers, P., Kiwi, J., 2003. Antibacterial textiles prepared by RF-plasma and vacuum-UV mediated deposition of silver. *J. Photochem. Photobiol. A Chem.* 161 (1), 27–34. [https://doi.org/10.1016/s1010-6030\(03\)00204-1](https://doi.org/10.1016/s1010-6030(03)00204-1).
- Zeng, G., Huang, L., Huang, Q., Liu, M., Xu, D., Huang, H., Yang, Z., Deng, F., Zhang, X., Wei, Y., 2018. Rapid synthesis of MoS<sub>2</sub>-PDA-Ag nanocomposites as heterogeneous catalysts and antimicrobial agents via microwave irradiation. *Appl. Surf. Sci.* 459, 588–595. <https://doi.org/10.1016/j.apsusc.2018.07.144>.
- Zhang, Y., Ding, H., Liu, Y., Pan, S., Luo, Y., Li, G., 2012. Facile one-step synthesis of plasmonic magnetic core shell nanostructures and their multifunctionality. *J. Mater. Chem.* 22 (21), 10779. <https://doi.org/10.1039/c2jm16293h>.
- Zhang, Y., Ahn, J., Liu, J., Qin, D., 2018. Syntheses, Plasmonic Properties, and Catalytic Applications of Ag–Rh Core-Frame Nanocubes and Rh Nanoboxes with Highly Porous Walls. *Chem. Mater.* 30 (6), 2151–2159. <https://doi.org/10.1021/acs.chemmater.8b00602>.
- Zhang, J., Pan, Y., Dong, S., Yang, M., Huang, Z., Yan, C., Gao, Y., 2023. Montmorillonite/Agarose Three-Dimensional Network Gel Sponge for Wound Healing with Hemostatic and Durable Antibacterial Properties. *ACS Appl. Nano Mater.* 6 (18), 17263–17275. <https://doi.org/10.1021/acsnm.3c03708>.
- Zhang, K., Wang, C., Rong, Z., Xiao, R., Zhou, Z., Wang, S., 2017. Silver coated magnetic microflowers as efficient and recyclable catalysts for catalytic reduction. *New J. Chem.* 41 (23), 14199–14208. <https://doi.org/10.1039/c7nj02802d>.
- Zhang, L., Wu, H.B., Lou, X.W., 2014. Iron-oxide-based advanced anode materials for lithium-ion batteries. *Adv. Energy Mater.* 4 (4), 1300958. <https://doi.org/10.1002/aenm.201300958>.
- Zhao, W., Feng, L., Yang, R., Zheng, J., Li, X., 2011. Synthesis, characterization, and photocatalytic properties of Ag modified hollow SiO<sub>2</sub>/TiO<sub>2</sub> hybrid microspheres. *Appl. Catal. B* 103 (1–2), 181–189. <https://doi.org/10.1016/j.apcatb.2011.01.025>.
- Zhao, R., Lv, M., Li, Y., Sun, M., Kong, W., Wang, L., Song, S., Fan, C., Jia, L., Qiu, S., Sun, Y., Song, H., Hao, R., 2017. Stable nanocomposite based on PEG ylated and silver nanoparticles loaded graphene oxide for long-term antibacterial activity. *ACS Appl. Mater. Interfaces* 9 (18), 15328–15341. <https://doi.org/10.1021/acsami.7b03987>.
- Zhao, X., Wang, R., Lu, Z., Wang, W., Yan, Y., 2019. Dual sensitization effect and conductive structure of Fe<sub>3</sub>O<sub>4</sub>@mTiO<sub>2</sub>/C photocatalyst towards superior photodegradation activity for bisphenol A under visible light. *J. Photochem. Photobiol. A Chem.* 382, 111902. <https://doi.org/10.1016/j.jphotochem.2019.111902>.
- Zheng, Y., Wang, A., 2012. Ag nanoparticle-entrapped hydrogel as promising material for catalytic reduction of organic dyes. *J. Mater. Chem.* 22 (32), 16552–16559. <https://doi.org/10.1039/C2JM32774K>.